WATER RESOURCES RESEARCH, VOL. 49, 1–21, doi:10.1002/wrcr.20495, 2013

Development of a deterministic downscaling algorithm for remote sensing soil moisture footprint using soil and vegetation classifications

Yongchul Shin[1] and Binayak P. Mohanty[1]

Received 27 June 2012; revised 29 July 2013; accepted 15 August 2013.

[1] Soil moisture (SM) at the local scale is required to account for small-scale spatial heterogeneity of land surface because many hydrological processes manifest at scales ranging from cm to km. Although remote sensing (RS) platforms provide large-scale soil moisture dynamics, scale discrepancy between observation scale (e.g., approximately several kilometers) and modeling scale (e.g., few hundred meters) leads to uncertainties in the performance of land surface hydrologic models. To overcome this drawback, we developed a new deterministic downscaling algorithm (DDA) for estimating fine-scale soil moisture with pixel-based RS soil moisture and evapotranspiration (ET) products using a genetic algorithm. This approach was evaluated under various synthetic and field experiments (Little Washita-LW 13 and 21, Oklahoma) conditions including homogeneous and heterogeneous land surface conditions composed of different soil textures and vegetations. Our algorithm is based on determining effective soil hydraulic properties for different subpixels within a RS pixel and estimating the long-term soil moisture dynamics of individual subpixels using the hydrological model with the extracted soil hydraulic parameters. The soil moisture dynamics of subpixels from synthetic experiments matched well with the observations under heterogeneous land surface condition, although uncertainties (Mean Bias Error, *MBE*: −0.073 to −0.049) exist. Field experiments have typically more variations due to weather conditions, measurement errors, unknown bottom boundary conditions, and scale discrepancy between remote sensing pixel and model grid resolution. However, the soil moisture estimates of individual subpixels (from the airborne Electronically Scanned Thinned Array Radiometer (ESTAR) footprints of 800 m × 800 m) downscaled by this approach matched well (*R*: 0.724 to −0.914, *MBE*: −0.203 to −0.169 for the LW 13; *R*: 0.343–0.865, *MBE*: −0.165 to −0.122 for the LW 21) with the in situ local scale soil moisture measurements during Southern Great Plains Experiment 1997 (SGP97). The good correspondence of observed soil water characteristics $\theta(h)$ functions (from the soil core samples) and genetic algorithm (GA) searched soil parameters at the LW 13 and 21 sites demonstrated the robustness of the algorithm. Although the algorithm is tested under limited conditions at field scale, this approach improves the availability of remotely sensed soil moisture product at finer resolution for various land surface and hydrological model applications.

Citation: Shin, Y., and B. P. Mohanty (2013), Development of a deterministic downscaling algorithm for remote sensing soil moisture footprint using soil and vegetation classifications, *Water Resour. Res.*, *49*, doi:10.1002/wrcr.20495.

1. Introduction

[2] Land surface soil moisture (SM) is a pivotal factor related to land-atmosphere interactions, surface runoff processes, and ground water recharge in hydrology. In general, in situ soil moisture data have the limited availability at the spatiotemporal scales. Point-scale soil moisture data sets are time consuming, expensive, and do not provide a uniform representation at larger scales. Remote sensing (RS) techniques can provide an attractive alternative to direct measurement. *Ottlé and Vidal-Madjar* [1994] derived land surface soil moisture using thermal infrared remote sensing. Directly active [*Ulaby et al*., 1996] and passive microwave [*Njoku and Entekkabi*, 1996] remote sensing approaches were developed to estimate surface soil moisture dynamics. However, the use of RS pixel-based data is limited due to the scale discrepancy between observed RS resolution and required modeling resolution [*Engman*, 1991; *Entekhabi et al*., 1999]. In this regard, downscaling schemes are

[1]Department of Biological and Agricultural Engineering, Texas A&M University, College Station, Texas, USA.

Corresponding author: B. P. Mohanty, Department of Biological and Agricultural Engineering, Texas A&M University, 301 C Scoates Hall, College Station, TX 77843-2117, USA.

0043-1397/13/10.1002/wrcr.20495

necessary to improve the availability of subpixel soil moisture products from RS footprints/pixels for agriculture and water resources management at the field scale.

[3] A few studies have explored downscaling or disaggregation methods for extracting subgrid soil moisture estimates within a RS pixel. *Crow et al*. [2000] downscaled spaceborne soil moisture products to obtain surface soil dielectric values approximating to volumetric soil moisture content using a soil dielectric inversion model. *Merlin et al*. [2005; 2012] developed a downscaling method using fine-scale optical data during the Soil Moisture and Ocean Salinity (SMOS) mission [*Kerr et al*., 2001] to improve the availability of SMOS near-surface soil moisture at the subgrid scale. Currently, visible/infrared RS data (i.e., normalized difference vegetation index-NDVI, land surface temperature, etc.) have been used in downscaling SMOS footprints [*Chauhan et al*., 2003; *Merlin et al*., 2008; *Piles et al*., 2010; *Piles et al*., 2011]. In their studies, high resolution soil moisture estimates were obtained by combining coarse-scale (i.e., 40 km $\times$ 40 km) SMOS soil moisture footprints to finer-scale (i.e., 1 km $\times$ 1 km) vegetation index and surface temperature data in the spatial domain based on regression models. Also, an interpolation approach of passive microwave data based on fine-scale active microwave data was developed by *Kim and Barros* [2002] and further refined by *Das et al*. [2008] particularly for the Soil moisture Active and Passive (SMAP) mission.

[4] From the hydrologic process point of view, both soil textures and evaporatranspiration (ET) influence soil moisture dynamics across the land surface because ET returns to the atmosphere via evaporation (E) and transpiration (T) [*Huxman et al*., 2005; *Boulet et al*., 1997; *van Keulen and Hillel*, 1974; *Yamanaka and Yonetani*, 1999]. In semiarid regions, E may account for more than half of ET [*Huxman et al*., 2005], while soil moisture is the main source of water for T in the entire root zone. This indicates that ET significantly influences the water cycle at the near surface and in the root zone [*Xevi et al*., 1996], but it has not been considered yet in scaling down RS soil moisture products. Various approaches have been developed for estimating spatially distributed ET such as Simplified Surface Energy Balance Index (S-SEBI) [*Roerink et al*., 2000], Mapping Evapotranspiration at high Resolution and with Internalized Calibration (METRIC) [*Allen et al*., 2007], Surface Energy Balance Algorithm for Land (SEBAL) [*Bastiaanssen et al*., 1998, 2005], and Surface Heat Budget of the Arctic Ocean (SHEBA) [*Su*, 2002], among others. Thus, spatially distributed ET values can be used to capture the variability of land surface within a RS pixel.

[5] Airborne/satellite-scale soil moisture footprints provide available large-scale applications, because of their spatiotemporal extents [*Kerr et al*., 2001; *Njoku et al*., 2003; *Entekhabi et al*., 2010; *Das et al*., 2011]. However, agricultural activities particularly occur at finer scale ranging from several hundred meters to several kilometers. To date, few studies have addressed the issue of downscaling remotely sensed soil moisture footprints (e.g., airborne Electronically Scanned Thinned Array Radiometer, ESTAR, Polarimetric Scanning Radiometer, PSR, space-borne Soil Moisture Ocean Salinity, SMOS, and Soil Moisture Active and Passive, SMAP sensors), and resolving them at fine scales (e.g., for individual fields with homogeneous soil and vegetation). *Mascaro et al*. [2010] suggested the predictive skill of land surface models to account for small-scale heterogeneity of soil moisture using a calibrated multifractal model during the Southern Great Plains experiment in 1997 (SGP97). *Ines et al*. [2013] developed a stochastic disaggregation method for soil moisture using a simulation-assimilation scheme. This approach extracts soil type identification (representing soil hydraulic properties) and subarea fractions of corresponding soil-vegetation combinations within a RS soil moisture product. However, the stochastic disaggregation method estimates only the soil characteristics (soil ID values) and subarea fractions (%) by the soil-vegetation combinations within a pixel in a probabilistic sense without their specific locations practically recognized. In order to realize the maximum potential of RS data, downscaling to the highest possible resolution is required [e.g., *Merlin et al*., 2008; *Das et al*., 2011]. Further, a few downscaling algorithms mentioned above can scale down airborne/satellite-scale soil moisture data at the spatial domain, but they still have limitations in providing continuous soil moisture dynamics with the time series.

[6] The main goal of this study is to develop and test a new downscaling algorithm with pixel-based soil moisture and evapotranspiration. The primary objectives are twofold: (1) to develop a deterministic downscaling algorithm (DDA) using a genetic algorithm (GA) scheme for producing subpixel level soil moisture products from large-spatial scale data in time continuous manner and (2) to assess the robustness of this approach for remotely sensed data under real and synthetic experiments across different hydroclimate conditions.

2. Materials and Methods

2.1. Deterministic Downscaling Algorithm (DDA)

[7] Heterogeneity across the land surface comprises different soil textures and vegetation covers (assuming the case of flat topography). Various soil-vegetation combinations have their unique characteristics of soil moisture and evapotranspiration dynamics as illustrated in Figure 1a. As we capture the distributed ET values of various soil-vegetation combinations within a pixel, the SM estimates and their locations corresponding to the distributed ET values can be obtained at subpixel levels. Here high resolution RS images provide finer-scale ET products across the land surface [*Roerink and Menenti*, 2000]. Thus, in this study we developed a deterministic downscaling algorithm (DDA) for extracting fine-scale soil moisture (for subpixels) within a RS footprint using pixel-based SM and ET.

[8] Basically, the spectral mixtures within a RS pixel-based product have linear relationships indicating that the response of each subpixel in any spectral wavelength can be considered as a linear combination of the responses of each component which is assumed to be in the mixture [*Holben and Shimabukuro*, 1993; *Ferreira et al*., 2007]. Thus, each image (subpixel) contains land surface information with respect to the fraction and spectral response of each component within the ground resolution unit. Hence, individual subpixel spectral images ($a_{i\,=\,1,\,\ldots\,M,j\,=\,1,\,\ldots,N}$), which have the soil components ($\boldsymbol{P}=\{\boldsymbol{s_{i,j}}\}$) in equation (1), can be practically designed as a linear mixture [*Ferreira et al*., 2007; *Ines et al*., 2013] (equations (2)–(4)) as below,

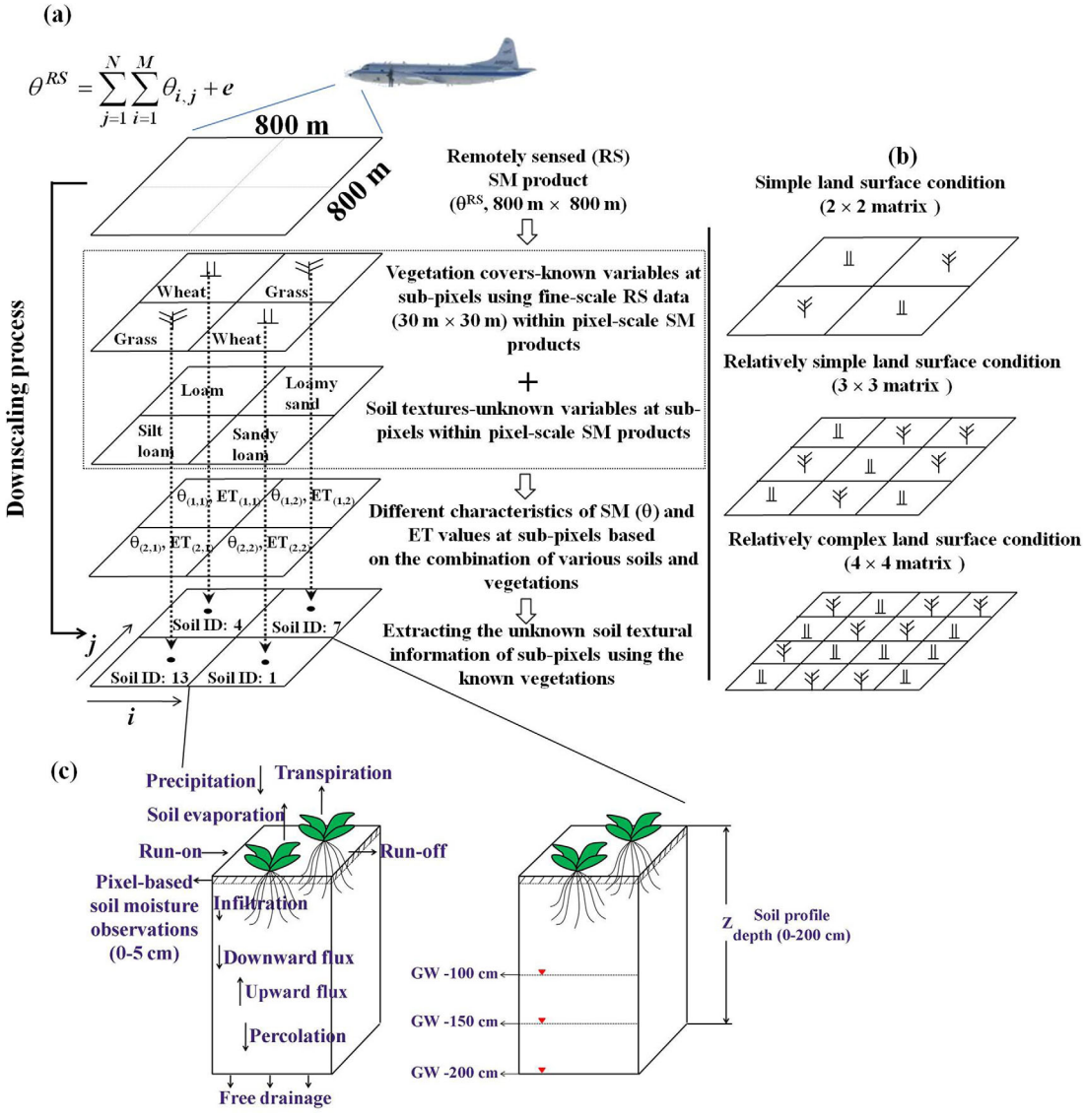

Figure 1. (a) Description of the deterministic downscaling algorithm, (b) simple (2 × 2 matrix), relatively simple (3 × 3 matrix), and relatively complex (4 × 4 matrix) land surface conditions, (c) homogeneous soil columns with the free drainage condition and various shallow ground water table depths (GW −200, −150, −100 cm).

$$\boldsymbol{P} = \left\{ s_{i,j} = s_{1,1}, \ldots, s_{M,N} \right\} \quad (1)$$

$$\theta^{avg,t}(\boldsymbol{P}) = \frac{1}{N}\frac{1}{M}\left\{ \sum_{j=1}^{N}\sum_{i=1}^{M} \theta^{sub,i,j,t} \right\} \quad \forall t \quad (2)$$

$$ET^{avg,t}(\boldsymbol{P}) = \frac{1}{N}\frac{1}{M}\left\{ \sum_{j=1}^{N}\sum_{i=1}^{M} ET^{sub,i,j,t} \right\} \quad \forall t \quad (3)$$

$$ET^{RSavg,t}(\boldsymbol{P}) = \frac{1}{N}\frac{1}{M}\left\{ \sum_{j=1}^{N}\sum_{i=1}^{M} ET^{RSsub,i,j,t} \right\} \quad \forall t \quad (4)$$

$$Min\boldsymbol{S}_{i,j} \le s_{i,j} \le Max\boldsymbol{S}_{i,j} \quad (5)$$

where $\boldsymbol{P}$: the variables whose $s_{i,j}$ component is the soil hydraulic properties of all the soil contained within the ij pixel, $\theta^{sub,i,j,t}$: the simulated soil moisture of individual subpixel in the time index (t), i: the row number of subpixels with the domain (M), j: the column number of subpixels with the domain (N), $\theta^{avg,t}$: the average soil moisture of individual subpixels ($\theta^{sub,i,j,t}$) in the time index (t), $ET^{sub,i,j,t}$: the simulated evapotranspiration of individual subpixel with the time index (t), $ET^{avg,t}$: the average evapotranspiration of individual subpixels ($ET^{sub,i,j,t}$) with the time index (t), $ET^{RSsub,i,j,t}$: the RS evapotranspiration product of individual subpixel with the time index (t), $ET^{RSavg,t}$: the average RS evapotranspiration products of individual subpixels ($ET^{RSsub,i,j,t}$) with the time index (t). The $s_{i,j}$ component can be constrained based on the number of soil textures available (see in Table 1) in equation (5).

[9] We used the unmixing model (equation (6)) designed to solve $\boldsymbol{P}$ ($s_{i,j}$ component) using a simulation-optimization

Table 1. Physical Soil Texture Database for the Deterministic Downscaling Algorithm

		Shape Parameters		Scaling Parameters		Hydraulic Conductivity	
Soil ID	Soil Textures	α	n	θ_{res}	θ_{sat}	K_{sat}	λ
1[a]	Sandy Loam	0.021	1.61	0.067	0.37	41.6	0.5
2[b]	Sandy Loam	0.075	1.89	0.065	0.41	106.1	0.5
3[c]	Sandy Loam	0.027	1.45	0.039	0.39	38.3	−0.861
4[a]	Loam	0.025	1.31	0.083	0.46	38.3	0.5
5[b]	Loam	0.036	1.56	0.078	0.43	25.0	0.5
6[c]	Loam	0.011	1.47	0.061	0.40	12.1	−0.371
7[a]	Silt	0.006	1.53	0.123	0.48	55.7	0.5
8[b]	Silt	0.016	1.37	0.034	0.46	60.0	0.5
9[c]	Silt	0.007	1.68	0.050	0.49	43.8	0.624
10[a]	Silt Loam	0.012	1.39	0.061	0.43	30.5	0.5
11[b]	Silt Loam	0.020	1.41	0.067	0.45	10.8	0.5
12[c]	Silt Loam	0.005	1.66	0.065	0.44	18.2	0.365
13[a]	Sandy Clay Loam	0.033	1.49	0.086	0.40	9.7	0.5
14[b]	Sandy Clay Loam	0.059	1.48	0.100	0.39	31.4	0.5
15[c]	Sandy Clay Loam	0.021	1.33	0.063	0.38	13.2	−1.280
16[a]	Clay Loam	0.030	1.37	0.129	0.47	1.8	0.5
17[b]	Clay Loam	0.019	1.31	0.095	0.41	6.2	0.5
18[c]	Clay Loam	0.016	1.42	0.079	0.44	8.2	−0.763
19[a]	Silty Clay Loam	0.027	1.41	0.098	0.55	7.4	0.5
20[b]	Silty Clay Loam	0.010	1.23	0.089	0.43	1.7	0.5
21[c]	Silty Clay Loam	0.008	1.52	0.090	0.48	11.1	−0.156
22[b]	Sandy Clay	0.027	1.23	0.100	0.38	2.9	0.5
23[c]	Sandy Clay	0.033	1.21	0.117	0.39	11.4	−3.665
24[a]	Silty Clay	0.023	1.39	0.163	0.47	8.4	0.5
25[b]	Silty Clay	0.005	1.09	0.070	0.36	0.5	0.5
26[c]	Silty Clay	0.016	1.32	0.111	0.48	9.6	−1.287
27[a]	Clay	0.021	1.20	0.102	0.51	26.0	0.5
28[b]	Clay	0.008	1.09	0.068	0.38	4.8	0.5
29[c]	Clay	0.015	1.25	0.098	0.46	14.8	−1.561

[a]UNSODA [*Leij et al*., 1999].
[b]SoilSurvey [Wösten *et al*., 1994].
[c]Rosetta [*Schaap et al*., 1999].

scheme based on inverse modeling [*Ines and Droogers*, 2002; *Ines and Mohanty*, 2008a, 2008b; *Ines and Mohanty*, 2009; *Shin et al*., 2012]. The unmixing model indicates that a RS soil moisture product ($\theta^{RS,t}$) can be estimated by the average simulated soil moisture ($\theta^{avg,t}(\boldsymbol{P})$) with adding an error term (e_t). As mentioned above, the classifications of different soils and vegetations have their own SM and ET characteristics. Hence, as we can obtain fine-scale remotely sensed ET estimates for individual subpixels, soil moisture corresponding to each ET value (that can represent soil texture) can be inferred as the disaggregated results. Thus, our approach extracts the soil components ($\boldsymbol{s_{i,j}}$) and their specific locations within a RS product by capturing the ET values ($ET^{avg,t}$) of individual subpixels. Then, an optimization scheme randomly generates the soil ID values for subpixels and searches for the solutions, which have the minimum differences between mixed/averaged (subpixels) observations and simulations (SM/ET) under the assumption that the exact solutions have no differences ($e_t = 0$). To minimize the error (e_t) between the observed versus simulated SM and ET by tuning a hydrological model, we used a genetic algorithm. The objective ($Z(\boldsymbol{P})$) and fitness ($Fitness(\boldsymbol{P})$) functions are shown in equations (7) and (8),

$$\boldsymbol{\theta^{RS,t}}(\boldsymbol{P}) = \boldsymbol{\theta^{avg,t}}(\boldsymbol{P}) + \boldsymbol{e_t} \quad \forall \boldsymbol{t} \tag{6}$$

$$Z(\boldsymbol{P}) = \mathrm{Min}\left\{\frac{1}{\boldsymbol{T}}\sum_{t=1}^{\boldsymbol{T}}\{\boldsymbol{f} \times |\boldsymbol{\theta^{avg,t}} - \boldsymbol{\theta^{RS,t}}| + (1-\boldsymbol{f}) \times |\boldsymbol{ET^{avg,t}} - \boldsymbol{ET^{RSavg,t}}|\}\right\} \tag{7}$$

$$Fitness(\boldsymbol{P}) = Max[Z(\boldsymbol{P})]^{-1} \tag{8}$$

where $\theta^{RS,t}$: the remotely sensed soil moisture product with the time index (t), $Z(\boldsymbol{P})$: The objective (minimizing) function (note that all variables were normalized based on their observation range), f: the weighting factor ($0 < f < 1.0$) indicating that the weighting factor of 0.1 means more weight is given to ET and the weighting factor of 0.9 means more weight to SM, and $Fitness(\boldsymbol{P})$: the maximization function if $Z(\boldsymbol{P})$ is minimized.

[10] This approach can disaggregate RS products at several kilometers scales, but each subpixel still has the variability across the land surface. In order to search effective soil parameters values that can represent the soil moisture dynamics of individual disaggregated subpixels, we used a genetic algorithm (GA)-based optimization. GAs are search algorithms to solve the optimized solutions for complex problems based on the survival of competing mechanism [*Holland*, 1975; *Goldberg*, 1989]. GAs are influenced by not only initial random generator seeds (i.e., −3000, −2000, −1000, etc.), but also by the number of parameters

(***P***) to be searched from unknown spaces. In this study, we selected the Ensemble Multiple Operators Genetic Algorithm (EMOGA) (Y. C. Shin, and B. P. Mohanty (2012), Development of drought severity assessment framework using remotely sensed soil moisture products with climate changes, submitted to *Water Resources Research*, 2013). The Multiple Operators Genetic Algorithm (MOGA) has the unique ability that reproduces the fittest chromosomes (***P***) in the individual population as much as the number of chromosomes (parameters: $M \times N$) to be searched (see Figure 2). The reproduced chromosomes ($RC = 1, \ldots, M \times N$) have new genetic information through the GA operators (selection, crossover, and mutation) and explore more search spaces. Then, the MOGA restarts when the chromosomes are converged to one region, which means that the better chromosomes are not searched compared to the previous strongest one for past 50 generations (note that the number of generations is subjective) at the converged region before the GA process is completed. With the restarting technique, the MOGA provides new genetic materials through the creep and jump mutation operators [*Ines and Honda*, 2005]. The MOGA always remembers the previous $(g-1)$ elite chromosomes and reproduce in the next generation [*Ines and Mohanty*, 2008a]. We integrated a random resampling (ensemble e) algorithm (IBM Programmers' Guide) [*Efron*, 1982] into the MOGA for searching more unknown spaces, called EMOGA. EMOGA generates the soil parameters (chromosomes) along the given generations for individual ensembles (e) with different random generator seeds. Then, the parameter set, which has the best fitness in the given generations, of each ensemble for different random generator seeds was selected and used for uncertainty analysis.

[11] This approach with the EMOGA uses a physically based (1-D) soil water atmosphere plant (SWAP) model to simulate soil water flow between the soil, water, atmosphere, and plant system [*Kroes et al*., 1999; *van Dam et al*., 1997]. The SWAP model calculates the soil water flow based on Richards' equation in equation (9).

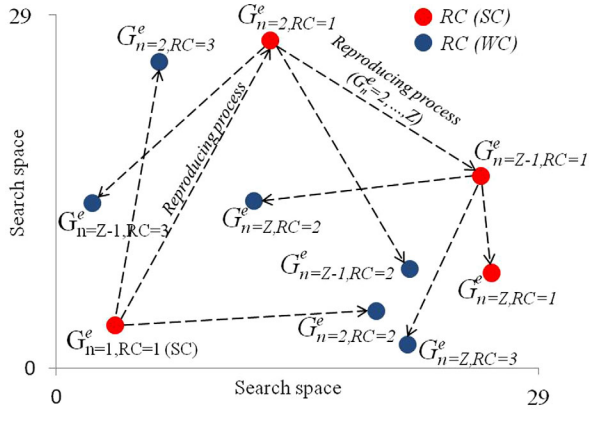

Figure 2. Schematic of ensemble multiple operators genetic algorithm (EMOGA) for searching the soil hydraulic parameters based on the resampling (ensemble) process in the unknown space.

$$\frac{\partial \boldsymbol{\theta}}{\partial \boldsymbol{t}} = \boldsymbol{C}(\boldsymbol{h})\frac{\partial \boldsymbol{h}}{\partial \boldsymbol{t}} = \frac{\partial\left[\boldsymbol{K}(\boldsymbol{h})\left(\frac{\partial \boldsymbol{h}}{\partial \boldsymbol{z}} + 1\right)\right]}{\partial \boldsymbol{z}} - \boldsymbol{S}(\boldsymbol{h}) \tag{9}$$

where θ: the soil moisture content ($cm^3\ cm^{-3}$), $K(h)$: the hydraulic conductivity ($cm\ d^{-1}$), h: the pressure head (cm), z: the soil depth (cm) taken positively upward, t: the time (d), $C(h)$: the differential water capacity (cm^{-1}), and $S(h)$: the actual soil moisture extraction rate by plants ($cm^3\ cm^{-3}\ d^{-1}$) defined as equation (10).

$$\boldsymbol{S}(\boldsymbol{h}) = \boldsymbol{\alpha}_{\boldsymbol{w}}(\boldsymbol{h})\frac{\boldsymbol{T}_{\boldsymbol{pot}}}{\boldsymbol{Z}_{\boldsymbol{r}}} \tag{10}$$

where T_{pot}: the potential transpiration ($cm\ d^{-1}$), Z_r: the rooting depth (cm), and α_w: the reduction factor as function of h and accounts for water deficit and oxygen stress [*Feddes et al*., 1978]. The soil hydraulic functions defined by the Mualem-van Genuchten equations [*van Genuchten*, 1980; *Mualem*, 1976] allow the use of soil hydraulic parameters as inputs to the SWAP model.

$$\boldsymbol{S}_{\boldsymbol{e}} = \frac{\boldsymbol{\theta}(\boldsymbol{h}) - \boldsymbol{\theta}_{\boldsymbol{res}}}{\boldsymbol{\theta}_{\boldsymbol{sat}} - \boldsymbol{\theta}_{\boldsymbol{res}}} = \left[\frac{1}{1 + |\boldsymbol{\alpha}\mathrm{h}|^{\boldsymbol{n}}}\right]^{\boldsymbol{m}} \tag{11}$$

$$\boldsymbol{K}(\boldsymbol{h}) = \boldsymbol{K}_{\boldsymbol{sat}}\boldsymbol{S}_{\boldsymbol{e}}^{\boldsymbol{\lambda}}[1 - (1 - \boldsymbol{S}_{\boldsymbol{e}}^{1/\boldsymbol{m}})^{\boldsymbol{m}}]^2 \tag{12}$$

where S_e: the relative saturation, θ_{res}: the residual water contents ($cm^3\ cm^{-3}$), and θ_{sat}: the saturated water contents ($cm^3\ cm^{-3}$), α (cm^{-1}), n, m, and λ: the shape parameters of the retention and the conductivity functions, K_{sat}: the saturated hydraulic conductivity ($cm\ d^{-1}$), and $m = 1 - 1/n$, respectively.

[12] The SWAP model considers various top and bottom boundary conditions such as weather conditions, water table depths, flux, and surface drain, etc. [*van Dam et al*., 1997]. The SWAP model has three crop routines: (i) a simple model to simulate the impacts of weather, soil feature, and plant type, (ii) a detailed model (WOFOST), and (iii) the same model attuned to simulate grass growth. In this study, we used the simple and detailed (WOFOST 6.0, see details in *Supit et al*. [1994]) models for grass and wheat, respectively. Also, water management modules (irrigation and drainage) are available in SWAP [*van Dam et al*., 1997; *van Dam*, 2000]. The SWAP model estimates the potential evapotranspiration (ET_{pot}) using the Penman-Monteith equation and partitions the potential transpiration (T_{pot}) and soil evaporation (E_{pot}) by the leaf area index or the soil cover fraction. ET_{pot} is estimated based on the minimum value of canopy resistance and actual resistance and then in turn ET_{act} is determined by the root water uptake reduction due to water and salinity stress. This hydrological model performs well under various meteorological conditions [*Wesseling and Kroes*, 1998; *Sarwar et al*., 2000; *Droogers et al*., 2000; *Singh et al*., 2006].

2.2. Physical Soil Texture Database

[13] When the land surface within a RS product is composed of several soil textures (e.g., sandy loam, silt loam, and clay loam, etc.), we traditionally need to search the effective soil hydraulic parameters (α, n, θ_{res}, θ_{sat}, K_{sat}) for each soil unit, which means that the parameter estimation

would take a large combinational problem. We suggest a physical soil texture database including various soil information from the UNSODA [*Leij et al*., 1999], Staring soil database [*Wösten et al*., 1994] and Rosetta [*Schaap et al*., 1999] in Table 1. This database contains the soil hydraulic properties (29 soil textures) of Mualem-van Genuchten functions. Using the physical soil texture database, the soil hydraulic information ($s_{i,j}$) corresponding to the soil ID values can be provided for individual soil unit in the model performance.

2.3. Simplified-Surface Energy Balance Index (S-SEBI) Model

[14] Evapotranspiration is the process by which liquid water evaporates from open water, soil, and plant surfaces to the atmosphere across the land-atmosphere boundary. Remote sensing measurements of the surface energy balance provide a means to evaluate spatially and temporally distributed vegetation conditions at large scales [*Moran et al*., 1995; *Moulin et al*., 1998]. In this study, we selected a Simplified-Surface Energy Balance Index (S-SEBI) model for calculating pixel-based evapotranspiration (ET, mm d^{-1}) estimates using RS products [*Roerink and Menenti*, 2000]. The land surface energy balance can be solved on a pixel by pixel basis using RS (e.g., LANDSAT-TM, Moderate Resolution Imaging Spectroradiometer, MODIS, Advanced Very High Resolution Radiometer, AVHRR, etc.) data sets. The land surface energy balance is given by,

$$R_n = G_0 + H + \lambda E \tag{13}$$

where, R_n: the net radiation [W/m^2], G_0: the soil heat flux [W/m^2], H: the sensible heat flux [W/m^2], and λE: the latent heat flux [W/m^2].

[15] The S-SEBI model uses scanned spectral radiance (visible, near-infrared, and thermal infrared range) for estimating surface reflectance, surface temperature, and vegetation index under clear weather conditions. We used the LANDSAT-TM images (30 m × 30 m) described in Table 2 to compute fine-scale pixel-based ET using the S-SEBI model.

2.4. Data Assimilation Framework

[16] In order to assess our proposed methodology, we conducted synthetic and field validation experiments under the rain-fed condition including: (i) Case 1—synthetic experiments with various land surface conditions, (ii) Case 2—impacts of different vegetation covers (assumed that the land surface has a uniform vegetation cover) and the presence of shallow ground water tables under the synthetic conditions, and (iii) Case 3—field validation experiments, respectively. The synthetic condition meant that the observed soil moisture dynamics were generated by the hydrological model simulations using the real weather data (i.e., precipitation, wind speed, maximum and minimum temperature, humidity, and solar radiation) and the reference soil parameters (α, n, θ_{res}, θ_{sat}, θ_{sat}) from literatures (i.e., UNSODA [*Leij et al*., 1999], Soil Survey [*Wösten et al*., 1994], Rosetta [*Schaap et al*., 1999], etc.) in a forward mode, while the in situ/RS soil moisture data were used as observations for the field validation experiments.

[17] In Case 1,we designed the synthetic (simple – 2 × 2 matrix, relatively simple – 3 × 3 matrix, and relatively complex – 4 × 4 matrix at the airborne footprint-scale, Figure 1b) land surface conditions representing homogeneous and heterogeneous land surface with free drainage (indicating semi/arid regions) at the Lubbock site (1 March to 31 July 2002) in Texas. Furthermore, we tested our approach under the complex (6 × 6 matrix) condition that can represent relatively larger-scale domains (compared to the other synthetic conditions above) including three different soil textures (sandy loam, silt loam, and clay loam) and vegetation covers (grass, maize, and wheat) in Figure 3.

[18] We collected the daily weather data sets (i.e., precipitation, wind speed, maximum and minimum temperature, and solar radiation) at the Irrigation Technology Center (http://texaset.tamu.edu/index.php). In this study, evapotranspiration component is the major factor for downscaling RS soil moisture products. To confirm the impact of ET component for the downscaling process, we analyzed the characteristics of (synthetic) soil moisture (0–1 cm) and ET dynamics by the combinations of different soil textures (see Table 1: i.e., Soil ID: 1—sandy loam, 4—loam, 7—silt, and 13—sandy clay loam) and various vegetation covers (wheat, soybean, grass, and maize). The various weighting factors (0.1–0.9) for the objective function (equation (7)) were also tested under the relatively simple land surface condition.

[19] Additional experiments were conducted to evaluate the impacts of various vegetation covers (wheat, soybean, grass, and maize) and varying the shallow ground water

Table 2. Description of the LANDSAT-TM Data

Image Character	Value
Sensor	LANDSAT-TM
Path/Row	28/36
Acquisition date (time)	20 Apr 1997 (16:35:29) 7 Jun 1997 (16:37:10) 9 Jul 1997 (16:38:16)
Reference system	UTM-24N
Resolution	Band 1–7 (30 m × 30 m)

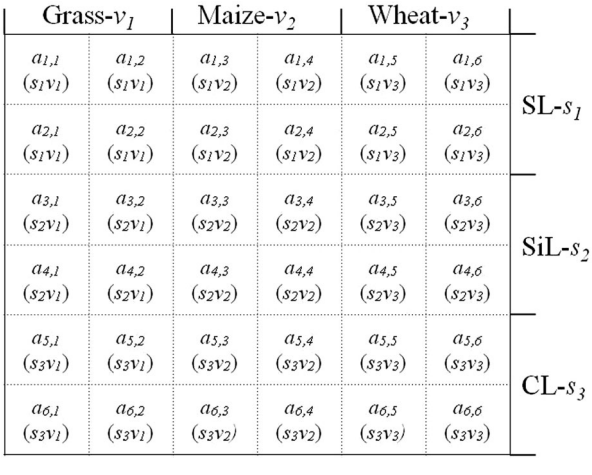

Figure 3. Grid domain for the complex land surface condition in Case 1 (6 × 6 matrix).

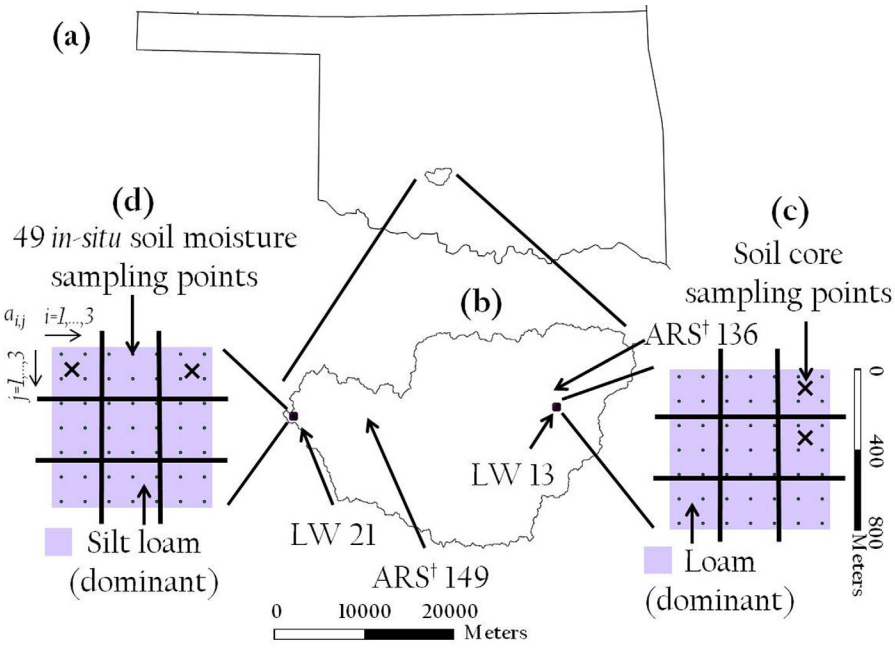

Figure 4. (a) Oklahoma, (b) Little Washita (LW) watershed, (c) LW 13 site, and (d) LW 21 site including the in situ soil moisture sampling points and weather stations for the field experiments.

table depths of −200, −150, and −100 cm (Figure 1c) under the relatively simple land surface condition for Case 2, respectively. The bottom flux (positive upward) is set to test that the interdependency assumption used in the inverse modeling is still executable when the soil water flow in the unsaturated zone is dominated by the bottom boundary condition, e.g., by major upward flows from the ground water table [*Walker et al*., 2001; *van Dam*, 2000].

[20] For the field validation experiments (Case 3), we selected the Little Washita watershed (LW 13 and 21 footprints) in Oklahoma during the simulation period (1 March to 31 July 1997) as shown in Figure 4. The in situ soil moisture data (0–5 cm) were measured during the Southern Great Plains experiment (SGP97) from 18 June 1997 to 18 July 1997 [*Mohanty and Skaggs*, 2001]. The daily volumetric soil moisture data sets (24/17 days for the LW 13/21 sites) were measured at the 49 (7 × 7) sampling points, except for the heavy rainfall events. We used the airborne Electronically Scanned Thin Array Radiometer (ESTAR, 800 m × 800 m) pixel-based soil moisture products for 17 days at the LW sites during the SGP97 period [*Jackson et al*., 1999]. This approach downscaled the ESTAR soil moisture products under the relatively simple land surface condition and was validated for subgrid (or subpixel) soil moisture values with the in situ soil moisture measurements. The soil core samples in the soil depth of 3–9 cm were collected to obtain the soil hydraulic properties [*Mohanty et al*., 2002] at the field sites. The subpixels $a_{1,3}$ and $a_{2,3}$ at the LW 13 site (Figure 4) have three and two soil core samples (i.e., soil hydraulic properties), respectively. Soil core samples at the subpixels $a_{1,1}$ and $a_{1,3}$ were taken at the LW 21 site. Besides soil moisture dynamics ($\theta(t)$) at the 49 in situ sampling locations for LW 13 and 21 (Figure 4), we further validated the downscaling approach through the comparison of (optimized versus observed) soil water retention functions ($\theta(h)$). They were derived by the searched soil ID values (in terms of their soil hydraulic parameters in Table 1) and field-observed soil hydraulic properties in Table 3. We excluded the hydraulic conductivity ($K(h)$) functions for validation, because of the extreme variations in K_{sat} (5.063–129.427 mm d^{-1}).

[21] The pixel-based ET (30 m × 30 m) estimates using the LANDSAT-TM data sets were computed by the S-SEBI model [*Roerink and Menenti*, 2000] for a few days

Table 3. Soil Hydraulic Properties Derived by the Soil Core Samples Obtained at the LW 13 and 21 Sites

Sites	Soil Depth	Subpixel ($a_{i,j}$)	α[a]	n[a]	θ_{res}[a]	θ_{sat}[a]	K_{sat}[a]
LW 13	3–9 cm	3 ($a_{1,3}$)	0.009	1.430	0.115	0.354	6.679
			0.015	1.204	0.002	0.322	5.063
			0.026	1.229	0.109	0.366	5.702
		6 ($a_{2,3}$)	0.012	1.262	0.106	0.435	129.427
			0.009	1.387	0.068	0.387	22.550
LW 21	3–9 cm	1 ($a_{1,1}$)	0.006	1.581	0.117	0.429	31.795
		3 ($a_{1,3}$)	0.009	1.734	0.115	0.432	17.885

[a]Field observations [*Mohanty et al*., 2002].

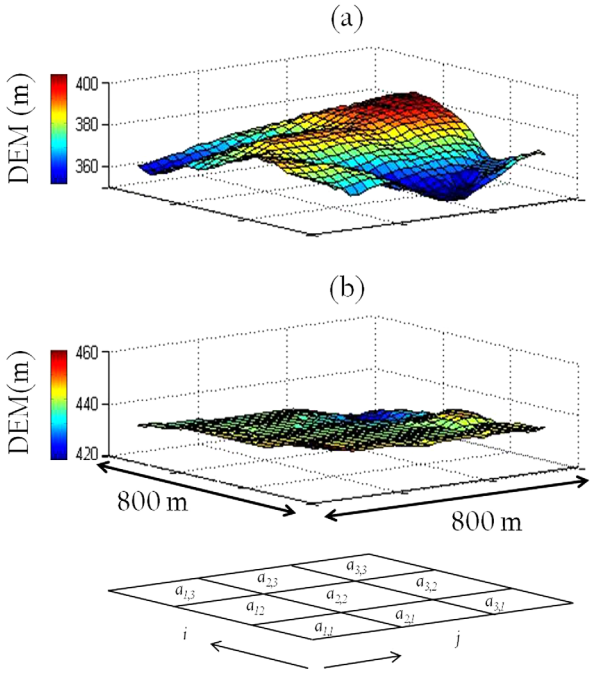

Figure 5. Digital elevation method (DEM) for the study sites at the Little Washita (LW) watershed in Oklahoma; (a) LW 13 site, (b) LW 21 site.

(i.e., 3 days for LW13 and 2 days for LW 21) during the simulation period due to the limited available LANDSAT-TM data sets and weather condition. The LW 13 and 21 sites have predominantly loam and silt loam soils from [*Mohanty et al*., 2002]. During the simulation period for the LW 21 site, two thirds were covered by the winter wheat, and the other third was covered by the short native grass. The wheat cover area is flat (slope less than 1%), and the grass cover area has a rolling slope (3–12%). The LW 13 site also has rolling topography with grass cover and a small pond in sub-pixel $a_{2,1}$ as shown in Figure 5. We set the different crop growing periods (1 March to 27 June for the wheat and grass cover at the LW 21 site and 1 March to 31 July for the LW 13 site), because wheat was harvested on 27 June at the LW 21 site. Daily climatic data sets for the model input were collected from the USDA-Agricultural Research Service micronet weather station (ARS 136/149 for the LW 13/21 sites, http://ars.mesonet.org/) in Oklahoma.

[22] In this study, we assumed that the remote sensing pixel (field) composed of parallel stream tubes or soil columns (subpixels) and the vertical soil columns are discretized by 33 texturally homogeneous computational layers. The soil profile was discretized at the intervals of 1 cm for the top 10 cm (1–10th layer) from the soil surface. For the soil depths of 10–60 cm (11–20th layer) and 60–200 cm (21–32nd layer), vertical grid intervals of 5 cm and 10 cm were used (except 20 cm in the 33rd layer). The initial conditions ($h(z,t = 0) = -100$ cm) were specified for the soil columns in the synthetic cases. We tested this approach under the free drainage and various ground water table depths (−200, −150, and −100 cm), because of the unknown bottom boundary conditions at the field sites. We assumed that the initial conditions were in equilibrium with the bottom boundary conditions. The model parameters used for genetic algorithm and SWAP for the synthetic and field validation experiments were shown in Table 4.

[23] For the uncertainty analysis, we used the simulation-optimization scheme (SWAP-EMOGA) with resampling (the number of ensemble members e) and multipopulation by various random generator seeds (−3000, −2000, and −1000) and respectively selected the maximum fitness for the individual simulations. Using the selected solutions ($e \times$ three different random seeds), we estimated the Pearson's correlation (R) and mean bias error (MBE). The ±95 percent confidence interval (95PCI) of the selected solutions was also calculated.

3. Results and Discussions

3.1. Synthetic Experiments: Various Land Surface Conditions

[24] The various combinations of soil textures (soil ID: 1, 4, 7, 13) and vegetation covers (wheat, soybean, grass, and maize) have their unique characteristics of soil water retention, soil hydraulic conductivity, soil moisture dynamics, and evapotranspiration as shown in Figure 6. The $\theta(h)$ and $K(h)$ functions of silt (ID: 7) soil were higher than those of loam (ID: 4), sandy clay loam (ID: 13), and sandy loam (ID: 1) soils (Figures 6a and 6b). Figures 6c and 6d show the impacts of various vegetation covers on estimating the SM and ET dynamics with a loam (ID: 4) soil.

Table 4. Modeling Conditions of Genetic Algorithm and SWAP Model

	Synthetic Experiments	Field Experiments
GA Parameters		
Number of population	30	30
Number of seed	−3000, −2000, −1000	−3000, −2000, −1000
Number of generation	5000	5000
Number of search restart	4 (relatively complex/complex conditions)	
Number of ensemble	10	10
Modeling Conditions		
Top boundary	Time-dependent flux/head	Time-dependent flux/head
Bottom boundary	Free drainage,	Free drainage,
	Ground water table	Ground water table
	Depth (−100, −150, −200 cm)	Depth (−100, −150, −200 cm)
Initial conditions	$h(z,t=0) = -100$ cm	Equilibrium with bottom boundary conditions

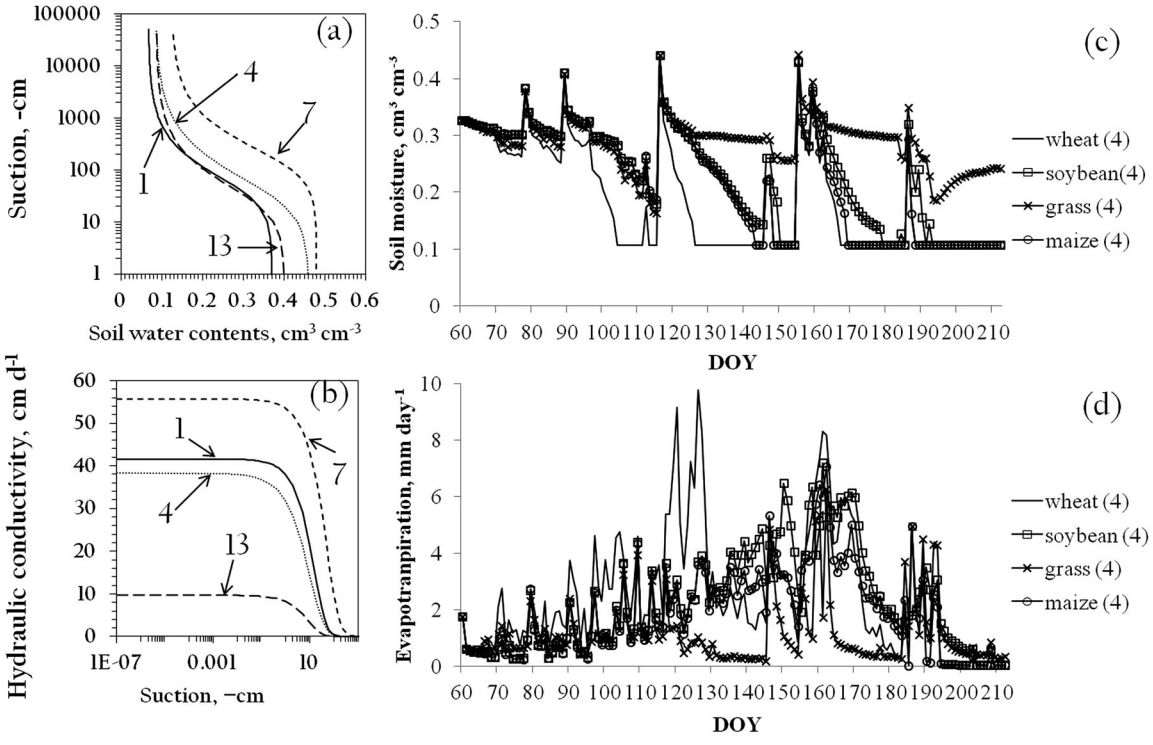

Figure 6. Various characteristics of the combinations of soil textures (soil ID: 1—sandy loam, 4—loam, 7—silt, and 13—sandy clay loam) and vegetation covers (wheat, soybean, grass, and maize); (a) soil water contents ($\theta(h)$), (b) hydraulic conductivities ($K(h)$), (c) soil moisture dynamics ($cm^3\ cm^{-3}$) for loam (4), (d) evapotranspiration ($mm\ day^{-1}$) for loam (4).

Overall, the grass cover with the average soil moisture (0.287 $cm^3\ cm^{-3}$) contains more moisture in the soil matrix than others (soybean—0.233, maize—0.221, and wheat—0.183 $cm^3\ cm^{-3}$) during the simulation period. However, average ET estimates (wheat—2.504, soybean—2.278, maize—1.866, and grass—1.159 $mm\ day^{-1}$) are contrary to the SM trends, except for the soybean cover, which has both relatively high SM and ET. It suggests that the vegetation covers influence not only the ET estimates but also soil moisture. In the context, *Pollacco and Mohanty* [2012] provided possibility of soil moisture and evapotranspiration coupling (or decoupling) at different soil moisture thresholds in the root zone.

[25] We tested the range of weighting factors f (0.1–0.9) for DDA with the relatively simple land surface condition in Case 1. When the weighting factors (f) were in the ranges of 0.1–0.5, the derived solutions were identified well with the synthetic observations in Table 5. The derived soil ID values ($s_{i=1,\ldots,3,j=1,\ldots,3}$) of individual subpixels with the weighting factor ($f=0.1$) have the highest fitness than others ($f=0.2$–0.5). But when more weights ($f=0.6$–0.9) were given to the soil moisture, the maximum

Table 5. Solutions (Soil ID) of Subpixels Derived by the Deterministic Downscaling Algorithm Using the Genetic Algorithm (EMOGA) Based on the Various Weighting Factors ($f=0.1$–0.9) Under the Relatively Simple Land Surface Condition for Case 1

		Relatively Simple Land Surface Condition								
		Weighting Factor								
Subpixel ($a_{i,j}$)	Observations (Soil ID)[a]	f=0.1	f=0.2	f=0.3	f=0.4	f=0.5	f=0.6	f=0.7	f=0.8	f=0.9
Maximum fitness		**1.11E + 07**	9.44E + 06	8.39E + 06	7.33E + 06	6.27E + 06	5.84E + 05	1.82E + 02	7.86E + 05	2.21E + 02
$a_{1,1}$	**4**	**4**	**4**	**4**	**4**	**4**	7	7	1	5
$a_{1,2}$	**7**	**7**	**7**	**7**	**7**	**7**	1	22	**7**	18
$a_{1,3}$	**13**	**13**	**13**	**13**	**13**	**13**	**13**	**13**	**13**	1
$a_{2,1}$	**1**	**1**	**1**	**1**	**1**	**1**	**1**	**1**	**1**	**1**
$a_{2,2}$	**4**	**4**	**4**	**4**	**4**	**4**	13	18	1	7
$a_{2,3}$	**7**	**7**	**7**	**7**	**7**	**7**	4	**7**	**7**	5
$a_{3,1}$	**13**	**13**	**13**	**13**	**13**	**13**	7	11	4	1
$a_{3,2}$	**1**	**1**	**1**	**1**	**1**	**1**	4	**1**	4	20
$a_{3,3}$	**1**	**1**	**1**	**1**	**1**	**1**	**1**	**1**	13	7

[a]Soil identification (soil ID) values from the physical soil texture database. Vegetation cover: wheat crop. Bold: the exact solution searched.

fitness decreased. Furthermore, the soil ID values for subpixels with the weighting factors ($f = 0.6$–0.8) were not matched well with the observations compared to the results for the weighting factors ($f = 0.1$–0.5). Most of all, the DDA showed good matching with the synthetic observations (soil ID), but the specific locations of derived soil ID values were not matched in the range of $f = 0.6$–0.9. It demonstrated that the ET component assigns the downscaled soil moisture estimates (by the searched soil ID values) of individual subpixels to the specific locations within a RS product. Thus, subsequently we used the selected weighting factor ($f = 0.1$) for the synthetic (Cases 1 and 2) and field validation experiments (Case 3).

[26] Table 6 shows the derived solutions (soil ID) under various land surface conditions in Case 1. The solutions for each subpixel are fairly well identified (minimum uncertainties) with the synthetic observations under the simple land surface condition. The results with the relatively simple land surface condition also matched well with the observations, even though they have small errors for subpixels ($a_{1,1}$, $a_{1,2}$, $a_{1,3}$, $a_{2,1}$, $a_{2,2}$, $a_{3,3}$). However, the uncertainty ranges of solutions increased considerably when the land surface condition becomes complex. The DDA approach found the exact soil ID values ($a_{1,1}$: 4, $a_{1,2}$: 7, $a_{1,3}$: 7, $a_{1,4}$: 13, $a_{2,1}$: 27, $a_{2,2}$: 4, $a_{2,3}$: 1, $a_{2,4}$: 20, $a_{3,1}$: 20, $a_{3,2}$: 7, $a_{3,3}$: 4, $a_{3,4}$: 7, $a_{4,1}$: 13, $a_{4,2}$: 27, $a_{4,3}$: 27, $a_{4,4}$: 1 from the physical soil texture database in Table 1) of subpixels, but the solution uncertainties for the relatively complex condition were considerably higher than those of the simple and relatively simple conditions. Figures 7 and 8 show the soil moisture dynamics (derived by the searched solutions in Table 4) estimated by this approach and ET for the subpixels under the relatively complex land surface condition (results for the simple and relatively simple conditions are not shown). The soil moisture dynamics of subpixels ($a_{1,1}$, $a_{2,2}$, and $a_{4,3}$) showed a bias compared to the observations as the mean bias error (*MBE*) were -0.031, -0.049, and 0.049, respectively. But the other subpixels matched well to the observations with -0.021 to -0.013 for the *MBE*. The simulated ET values tend to show similar pattern as the results of soil moisture, where the subpixels ($a_{1,1}$, $a_{2,2}$, and $a_{4,3}$) have more uncertainties (*MBE*: -0.009, -0.014, and -0.011) than those of the other pixels (*MBE*: -0.006 to 0.000). From the results for the subpixels of $a_{1,2}$ (silt and soybean), $a_{1,3}$ (silt and wheat), and $a_{2,2}$ (loam and soybean), we confirmed that different vegetation covers of subpixels (soybean for $a_{1,2}$ and wheat for $a_{1,3}$) with the same soil texture (ID: 7) influence not only the soil moisture, but also ET estimates. Soil moisture dynamics of subpixels ($a_{1,2}$ and $a_{2,2}$) with different soil textures (ID: 4, 7), which have the same vegetation cover (soybean), were affected by different soil textures (silt versus loam), but these soils have relatively less impacts on the ET dynamics. On the basis of above findings, we suggest that the ET component is the key factor for the proposed downscaling approach.

[27] Additionally, we tested our approach under the complex condition (that can represent larger scales) composed of three different soils (sandy loam, silt loam, and clay loam) and vegetations (grass, maize, and wheat) in Table 7. The model outputs had more uncertainties compared to those of the simple, relatively simple, and relatively complex conditions. For this reason, we calculated the average of fitness for the ensemble ($e = 10$) results (as the unfiltered) and only selected the solutions (as the filtered) above the average fitness value. Our approach found the filtered/unfiltered soil ID values well at the subpixels for sandy loam ($a_{i=1,..,2,j=1,\ldots,6}$) and clay loam ($a_{i=5,..,6,j=1,\ldots,6}$) soils with small uncertainties, but silt loam soil ($a_{i=3,..,4,j=1,\ldots,6}$) had relatively more uncertainties (especially for $a_{i=3,j=1}$). Also, the model outputs for the grass cover with silt loam soil showed limitations in extracting

Table 6. Solutions (Soil ID) Derived by the Deterministic Downscaling Algorithm Using the Genetic Algorithm (EMOGA) Under the Simple, Relatively Simple, and Relatively Complex Land Surface Conditions for Case 1

	Simplex Land Surface Condition			Relatively Simple Land Surface Condition			Relatively Complex Land Surface Condition		
Subpixel ($a_{i,j}$)	Observations (Soil ID)[a]	Vegetation cover[b]	Solution (Soil ID)	Observations (Soil ID)[a]	Vegetation cover[b]	Solution (Soil ID)	Observations (Soil ID)[a]	Vegetation cover[b]	Solution (Soil ID)
$a_{1,1}$	**4**	1–4	**4**	**4**	1	**4,7**	**4**	1	**4**,27
$a_{1,2}$	**7**	1–4	**7**	**7**	1	**4,7**	**7**	2	**7**,15,27
$a_{1,3}$				**13**	1	1,**13**	**7**	1	6,**7**,26,29
$a_{1,4}$							**13**	1	5, **13**
$a_{2,1}$	**13**	1–4	**13**	**1**	1	**1**,4	**27**	2	4,10,**27**
$a_{2,2}$	**1**	1–4	**1**	**4**	1	**4**,13	**4**	2	**4**,7,10,27
$a_{2,3}$				**7**	1	**7**	**1**	1	**1**
$a_{2,4}$							**20**	1	**20**
$a_{3,1}$				**13**	1	**13**	**20**	2	4,**20**,27
$a_{3,2}$				**1**	1	**1**	**7**	2	**7**,27
$a_{3,3}$				**1**	1	**1,**13	**4**	1	**4**,27
$a_{3,4}$							**7**	1	6,**7**,29
$a_{4,1}$							**13**	1	5,**13**
$a_{4,2}$							**27**	2	10,11,20,**27**
$a_{4,3}$							**27**	2	4,7,8,10,11,18,**27**,28
$a_{4,4}$							**1**	1	**1**

[a]Soil identification (soil ID) values from the physical soil texture database.
[b]Vegetation covers: 1—wheat, 2—soybean, 3—grass, 4—maize. Bold: the exact solution searched.

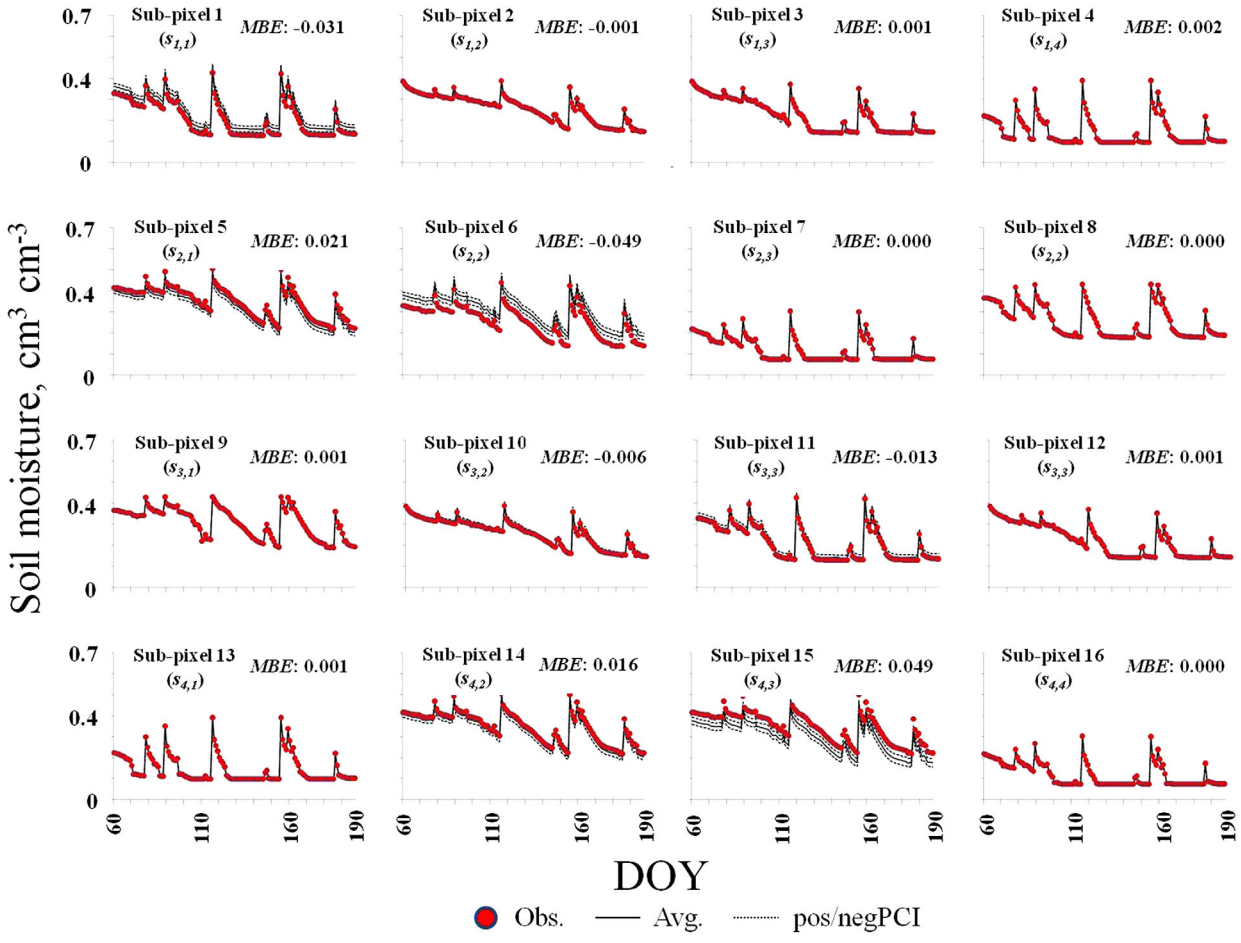

Figure 7. Soil moisture dynamics (0–1 cm) of subpixels downscaled by the deterministic downscaling algorithm using the genetic algorithm (EMOGA) under the relatively complex land surface condition for Case 1.

the soil ID information compared to maize and wheat. It might indicate that silt loam soil causes larger uncertainties in the model performance compared to others as shown in the findings of *Ines and Mohanty* [2008a] and *Shin et al.* [2013]. Although the unfiltered solutions had uncertainties for silt loam soil, the filtered ones could provide the more reliable disaggregated results for individual subpixels. Based on the filtered solutions, we compared the observed and estimated soil moisture dynamics in Figure 9. Note that we added the ±30% errors of the averaged (filtered) ensemble results to provide the reliable uncertainty ranges, and the ET results were excluded for the sake of brevity. As shown in Table 7, the estimated soil moisture dynamics (filtered) at the subpixels with sandy loam ($a_{i=1,..,2,j=1,\ldots,6}$) and clay loam ($a_{i=5,..,6,j=1,\ldots,6}$) soils perfectly matched the observations with R (1.000) and *MBE* (0.000), but silt loam soil had the relatively lower statistics (R: 0.946–1.000 and *MBE*: −0.073 to 0.032). Although the observed/simulated soil moisture dynamics were compared based on the filtered solutions under the complex land surface condition, these findings supported that our approach can be extended to satellite-scale soil moisture footprints (i.e., 25 km × 25 km, 40 km × 40 km, etc.) in future.

3.2. Impacts of Various Vegetation Covers and Shallow Ground Water Tables

[28] Table 8 shows the results of various vegetation covers (wheat, soybean, grass, and maize) under the synthetic condition in Case 2. Overall, the DDA approach searched well the soil ID values of subpixels with various land covers under the relatively simple condition, although the solutions with the wheat and soybean covers have more uncertainties than those of the grass and maize crops. The derived soil ID values for the maize cover perfectly matched with the synthetic observations. The results with different water table depths (−200, −150, and −100 cm) showed somewhat the similar trend with those of the free drainage condition (Table 9). The solutions with the GW −100 cm had more variations than those of GW −150 cm indicating that the estimations of soil parameters are affected due to the upward flow of shallow ground water table. The soil ID values with the GW −200 cm relatively had less uncertainties in modeling, but the results (ID: 1-sandy loam) of subpixels ($a_{1,1}$ and $a_{2,2}$) were not matched with the observation (ID: 4-Loam). The soil ID values (ID: 1, 4) had the similar soil hydraulic properties (see Table 1) indicating that this approach can be affected by the

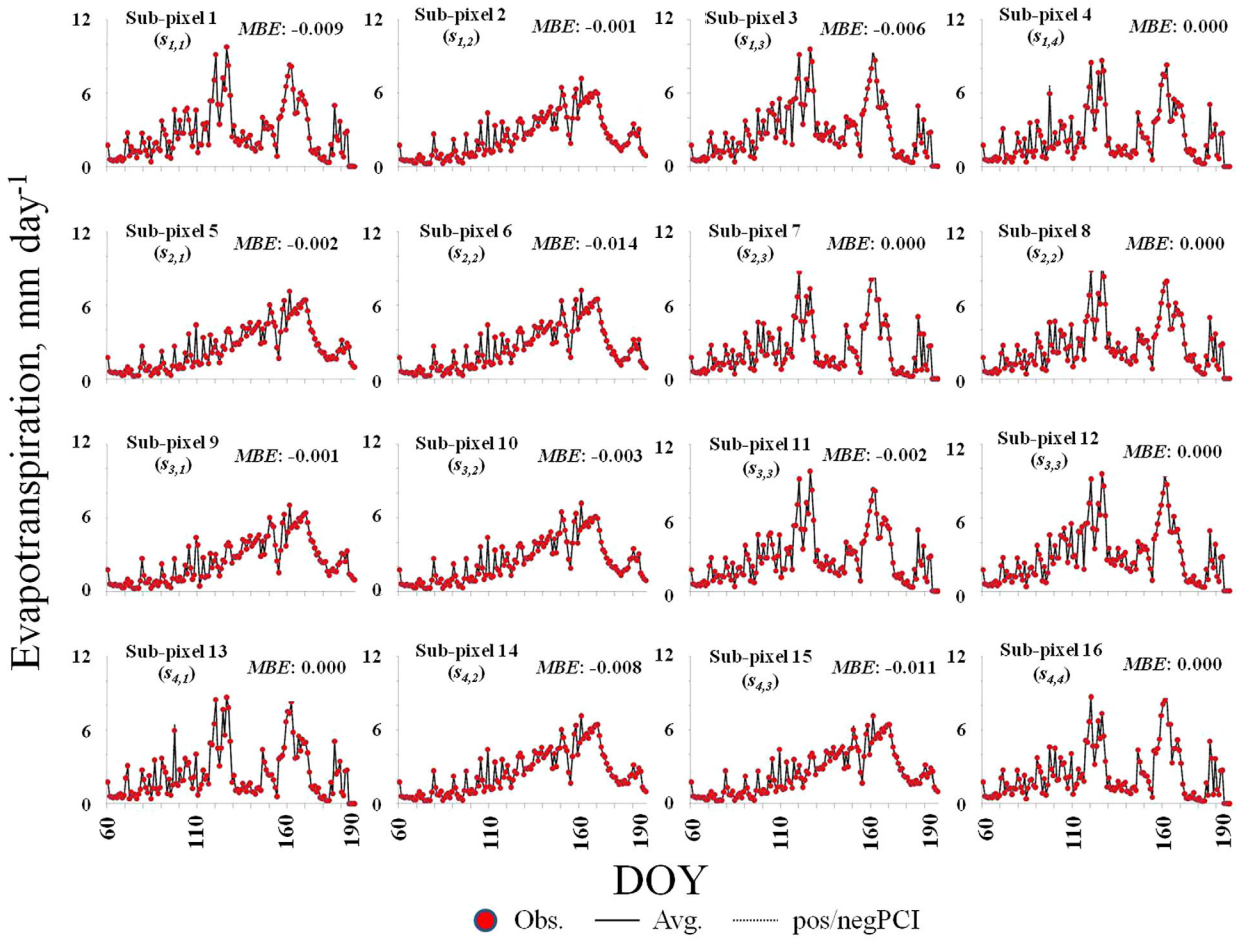

Figure 8. Evapotranspiration of subpixels by the deterministic downscaling algorithm using the genetic algorithm (EMOGA) under the relatively complex land surface condition for Case 1.

nonsensitivity of the similar soil water content ($\theta(h)$) and hydraulic conductivity ($K(h)$) functions. Overall, the impacts of shallow ground water tables were less sensitive than the vegetation covers, which mean that the land surface conditions (e.g., soil textures, land covers, atmospheric condition, etc.) influence this approach more than the shallow ground water tables.

3.3. Field Validation Experiments

[29] Figure 10 shows the statistics (maximum, minimum, median, and first/third quartiles of solutions) of model performance with free drainage condition and various ground water table depths for the field validation experiments in Case 3. We tested various bottom boundary conditions for the field sites under the free drainage and ground water tables (−200, −150, and −100 cm) in modeling, and the derived solutions for the ground water depth (GW) of −100 cm and free drainage condition at the LW 13 and 21 sites identified better with the measurements than those of the other conditions, respectively. Thus, we selected the bottom boundary conditions of GW −100 cm (LW 13) and free drainage (LW 21) for the field sites. The soil ID values derived by this approach were shown in Table 10. The solutions (soil ID values) of subpixels vary across the range of sandy loam (ID: 2, 3), loam (ID: 6), silt (ID: 8), silt loam (ID: 10), and silty clay loam (ID: 21) at the LW 13 site. However, loam and silt soils (ID: 6, 8) were dominant (60.0–90.0%) in the solutions of subpixels compared to the actual soil textures (loam predominantly, sandy loam, and silt loam soils). Similar trends were also shown in the results of the LW 21 site. The range of derived solutions including sandy loam (ID: 1, 2, 3), loam (ID: 5), silt (ID: 7, 9), silt loam (ID: 12), and sandy clay loam (ID: 13, 14) is more variable than those of the LW 13 site. As mentioned above, the soil water retention ($\theta(h)$) and hydraulic conductivity ($K(h)$) curves from the physical soil texture database across a range of pressure heads have similarity indicating that the search of soil textures (soil ID values) by this approach can be limited due to the nonsensitivity of $\theta(h)$ and $K(h)$ functions (as in Figure 11). However, this approach still searched silt and silt loam soils (ID: 7, 9, 12) as the dominant soils (36.7–73.3%) for the individual subpixels, except for the subpixels of $a_{2,1}$ and $a_{2,3}$. When we compared the solutions at the LW 13 and 21 sites, a sandy clay loam soil (ID: 14) was relatively more prominent in the derived solutions ($a_{1,1}$ and $a_{2,1}$) at the LW 21 site. This is because soil moisture at the LW 21 site were measured only for 17 days during the dry season indicating that the

Table 7. Solutions (Soil ID) Derived by the Deterministic Downscaling Algorithm Using the Genetic Algorithm (EMOGA) Under the Complex Land Surface Condition for Case 1[a]

	j=1 (v_1)		j=2 (v_1)		J=3 (v_2)		j=4 (v_2)		j=5 (v_3)		j=6 (v_3)	
$a_{i,j}$	Filtered	Unfiltered	Filtered	Unfiltered	Filtered	Unfiltered	Filtered	Unfiltered	Filtered	Unfiltered	Filtered	Unfiltered
i=1 (s_1)	**1**	**1**,19,28	**1**	**1**,17	**1**	**1**	**1**	**1**	**1**	**1**,13	**1**	**1**
i=2 (s_1)	**1**	**1**,20	**1**	**1**,20,29	**1**	**1**,13	**1**	**1**	**1**	**1**,13	**1**	**1**,17
i=3 (s_2)	3,15,18,26	3,6,8,15,18, 26,27,29	6,9,**10**,18	3,6,9,**10**, 12,18,26	6,**10**	6,**10**,26	6,8,**10**	6,8,**10**,29	6,8,**10**,29	6,8,**10**, 19,20,29	6,**10**, 15,18	6,8,**10**,15, 18
i=4 (s_2)	3,**10**,8,26	3,4,9,**10**, 15,18,26	7,9,**10**, 15,21	7,8,9,**10**, 15,21	**10**,18	6,**10**,18, 26	8,**10**	4,8,18,26	6,**10**,18	6,9,**10**,18	**10**,18,27	4,8,**10**,11, 18,19,27
i=5 (s_3)	**16**	9,13,**16**	**16**	13,14,**16**	**16**	**16**	13,**16**	13,**16**	13,**16**	13,**16**	**16**	3,5,**16**
i=6 (s_3)	**16**	13,**16**	**16**	2,13,**16**	**16**	13,**16**	**16**	13,**16**	**16**	1,**16**,22	**16**	13,**16**

[a]Filtered indicates the solutions selected above the average of 10 ensemble solutions. Unfiltered indicates the 10 ensemble solutions. s_1: sandy loam, s_2: silt loam, s_3: clay loam, v_1: grass, v_2: maize, v_3: wheat. Bold: the exact solution searched.

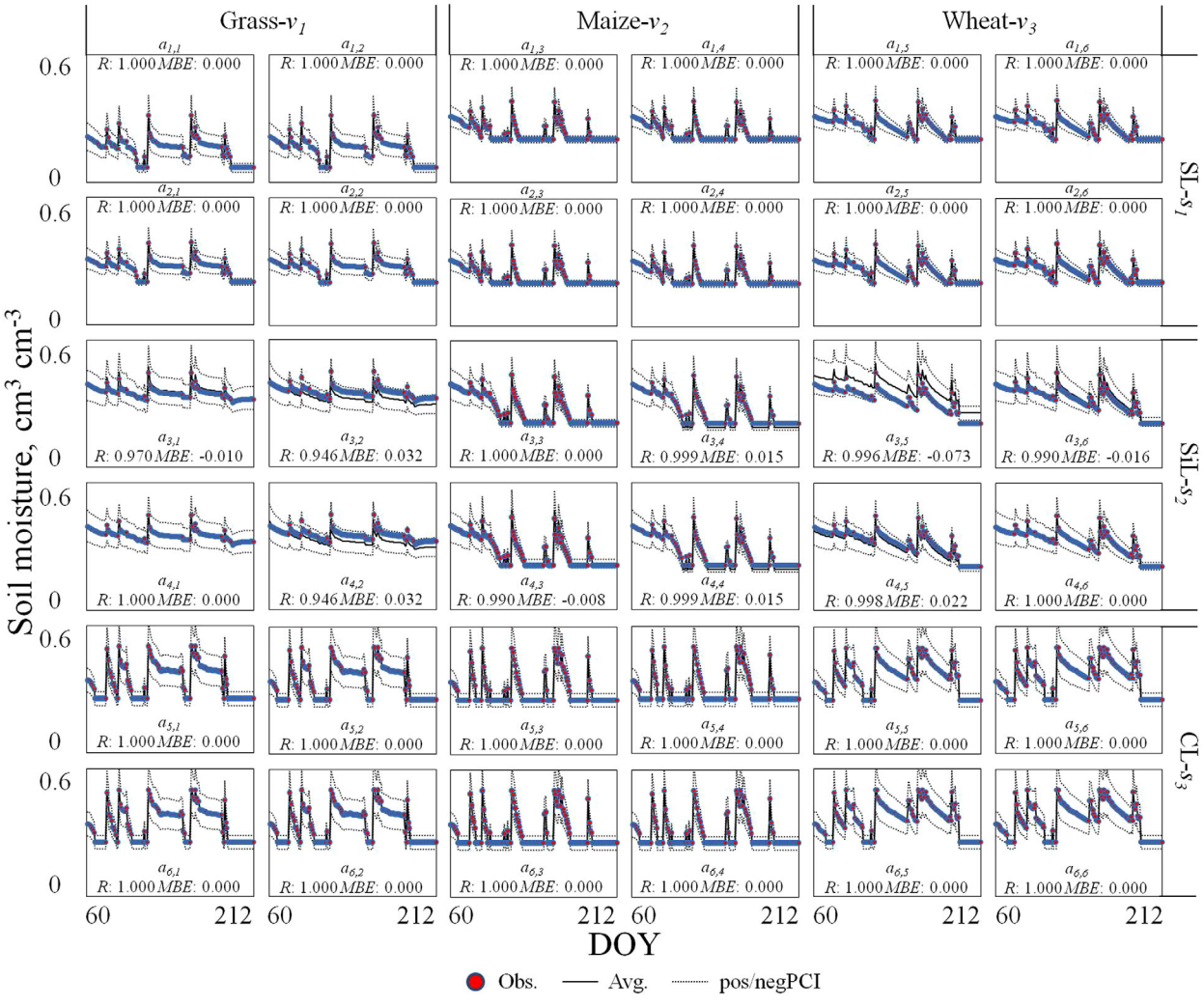

Figure 9. Soil moisture dynamics (0–1 cm) of subpixels downscaled by the deterministic algorithm using the genetic algorithm (EMOGA) under the complex land surface condition for Case 1.

Table 8. Solutions (Soil ID) Derived by the Deterministic Downscaling Algorithm Using the Genetic Algorithm (EMOGA) With Various Vegetation Covers (Wheat, Soybean, Grass, and Maize) Under the Relatively Simple Land Surface Condition for Case 2

		Relatively Simple Land Surface Condition			
Subpixel ($a_{i,j}$)	Observations[a] (Soil ID)	Wheat	Soybean	Grass	Maize
$a_{1,1}$	**4**	**4**	**4**	**4**,10,18	**4**
$a_{1,2}$	**7**	**7**,10	**7**	**7**	**7**
$a_{1,3}$	**13**	1,5,**13**	7,**13**	**13**	**13**
$a_{2,1}$	**1**	**1**,4	**1**,13	**1**	**1**
$a_{2,2}$	**4**	**4**,13	**4**,27	**4**	**4**
$a_{2,3}$	**7**	**7**,10	4,**7**,13	**7**	**7**
$a_{3,1}$	**13**	**13**	1,7,**13**	**13**	**13**
$a_{3,2}$	**1**	**1**	**1**	**1**	**1**
$a_{3,3}$	**1**	**1**	**1**	**1**	**1**

[a]Soil identification (soil ID) values from the physical soil texture database. Bold: the exact solution searched.

actual soil conditions could favor more a sandy or sandy clay loam soil. On the contrary, the LW 13 site has a small pond (subpixel: $a_{2,1}$) as shown in Figure 5, which means that the actual field site has more moisture explaining better solutions for the shallow GW of −100 cm than the others. Thus, it is not unusual that this approach searched different soil ID values, even though the field sites have similar soil textures.

[30] Figure 12a shows the measured (in situ) and downscaled soil moisture dynamics of subpixels ($a_{i:1,..,3,j:1,..,3}$) at the LW 21 site. Overall, the approach downscaled reasonably well the soil moisture estimates (R: 0.343–0.865 and MBE: −0.165 to −0.122) for the individual subpixels with the measurements, although the soil moisture values in the subpixels ($a_{1,3}$, $a_{2,2}$, $a_{3,1}$) have uncertainties (below 0.1 cm^3 cm^{-3}). The lowest soil moisture simulated by the hydrological model was about 0.1 (cm^3 cm^{-3}), but the in situ soil moisture measurements are even lower than the simulated estimates (<0.1 cm^3 cm^{-3}), which means that the hydrological model is less sensitive during the dry condition. We also compared the $\theta(h)$ functions derived by the dominant soil ID values (ID: 9, 14 for the subpixel $a_{1,1}$, and ID: 9, 12 for the subpixel $a_{1,3}$) for the individual subpixels with the observed $\theta(h)$ functions measured with the soil core samples collected at the LW 21 sites (shown in Figures 12b and 12c). The derived $\theta(h)$ functions, which have silt (ID: 9) and silt loam (ID: 12) soils, in the subpixel $a_{1,3}$ matched well with the observed soil water retention curve, but the $\theta(h)$ functions of subpixel $a_{1,1}$ have a bias compared to the observation, especially for sandy clay loam (ID: 14) soil. Pixel-based simulated ET estimates for the LW 21 site were illustrated in the Figure 13. The simulated ET estimates (MBE: −4.378 to −3.630, R is excluded, because of few data sets) with a wheat crop (at the subpixels $a_{1,2}$, $a_{1,3}$, $a_{2,2}$, $a_{2,3}$, $a_{3,2}$, $a_{3,3}$) are higher than those of the grass cover (subpixels: $a_{1,1}$, $a_{2,1}$, $a_{3,1}$). On DOY 190, ET was relatively underestimated compared to the observations, because wheat crop was harvested at the LW 21 site on 27 June (DOY 178) and converted to bare ground. Overall, although DDA estimated soil moisture and ET at subpixel level have errors due to inherent weaknesses of the adopted hydrological model (SWAP) and limited field measurements, the approach generally shows good performance for downscaling the remote sensing (ESTAR with 800 m × 800 m footprints) soil moisture products.

[31] The downscaled soil moisture dynamics (MBE: −0.203 to −0.169) at the LW 13 site showed more variations than those (MBE: −0.165 to −0.122) of the LW 21 site, although the correlations (R: 0.724–0.914) for LW13 are better than those (R: 0.343–0.865) for the LW 21 site in Figure 14a. The simulated soil moisture for the subpixels ($a_{1,1}$, $a_{1,2}$, $a_{1,3}$, $a_{2,1}$, $a_{2,3}$, $a_{3,1}$) are underestimated compared to the in situ measurements ($a_{1,1}$, $a_{1,2}$, $a_{1,3}$, $a_{2,1}$, $a_{2,3}$, $a_{3,1}$) at LW13. We suggest that as the land surface at the LW 13 site has a significant slope compared to the flat terrain of LW 21 site (<2% slope) indicating that topography causes

Table 9. Solutions (Soil ID) Derived by the Deterministic Downscaling Algorithm Using the Genetic Algorithm (EMOGA) for Different (Shallow) Ground Water Table Depths (−200, −150, and −100 cm) With the Wheat Crop Under the Relatively Simple Land Surface Condition for Case 2

Subpixel ($a_{i,j}$)	Observations[a] (Soil ID)	GW—100 cm	GW—150 cm	GW—200 cm
$a_{1,1}$	**4**	**4**,27	**4**	1
$a_{1,2}$	**7**	**7**,12	**7**,9,12	**7**,12
$a_{1,3}$	**13**	**13**	**13**	**13**
$a_{2,1}$	**1**	**1**	**1**	**1**
$a_{2,2}$	**4**	**4**,27	**4**	1
$a_{2,3}$	**7**	**7**,9,12	**7**,9,12	**7**,12
$a_{3,1}$	**13**	5,**13**	**13**	1,**13**
$a_{3,2}$	**1**	**1**	**1**	**1**,13
$a_{3,3}$	**1**	**1**	**1**	**1**

[a]Soil identification (soil ID) values from the physical soil texture database. Bold: the exact solution searched.

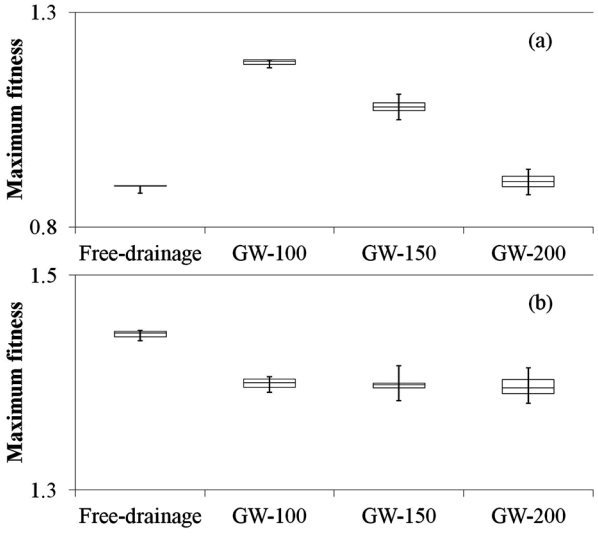

Figure 10. Maximum fitness of the field experiments (10 ensembles × three different random number generator seeds) with the various bottom boundary conditions (free drainage condition and GW−100, −150, −200 cm); (a) LW 13 site, (b) LW 21 site.

more uncertainties in downscaling of the RS soil moisture products than for a flat site. The derived $\theta(h)$ functions with the solutions (ID: 8-dominant, silt soil) of the subpixels (3 and 6) are compared with the observations in Figures 14b and 14c. The estimated $\theta(h)$ function in the subpixel 6 ($a_{1,3}$) somewhat corresponded well to the observed $\theta(h)$ function, but the water retention curve in the subpixel 3 ($a_{2,3}$) deviated from the observed curve. Overall, the simulated ET estimates matched the pixel-based ET with the correlations (R: 0.368–0.990) and uncertainties (MBE: −4.652 to −4.171). However, pixel-based ET estimation of subpixel ($a_{3,1}$) on DOY 158 was considerably higher than other values estimated by the S-SEBI model (Figure 15), because of a noise within the pixel and the presence of a small pond. The presence of pond is ignored during hydrologic model simulation. In summary, the DDA approach has uncertainties for extracting the soil ID values of subpixels within the RS soil moisture footprints based on certain landscape features that are not accounted in the hydrologic model. However, the $\theta(h)$ functions, soil moisture dynamics $\theta(t)$, and ET(t) estimates of individual subpixels matched reasonably well with the observations and demonstrated the applicability of our approach at the field scale. Our proposed approach has been validated under the limited conditions due to the lack of measurements. However, this algorithm could provide the reliable downscaled results using the limited RS data in a real world condition. Future field studies can be designed to implement and test this algorithm at much larger scale for (recently deployed and upcoming) satellite-based soil moisture (e.g., European Space Agency's SMOS, NASA's SMAP) platforms. While the approach should theoretically work on any flat landscapes, uncertainty due to complex terrains and additional computational demand for downscaling from such large footprints (e.g., 40 km × 40 km) need to be evaluated. Further, different remote sensing based evapotranspiration algorithms have been developed in the recent years with inherent limitations and advantages. Difference in algorithms might cause uncertainties in pixel-scale ET values. Comparison across different remote sensing based ET algorithms could be explored in the future in the context of the performance of the proposed downscaling algorithm.

4. Concluding Remarks

[32] We developed a deterministic downscaling algorithm using the ensemble multiple operators genetic algorithm (EMOGA) for estimating the (subpixel) finer-scale

Table 10. Solutions (Soil ID) Derived by the Deterministic Downscaling Algorithm Using the Genetic Algorithm (EMOGA) at the LW 13 and 21 Sites for Case 3[a]

	Subpixel ($a_{i,j}$)																	
	$a_{1,1}$		$a_{1,2}$		$a_{1,3}$		$a_{2,1}$		$a_{2,2}$		$a_{2,3}$		$a_{3,1}$		$a_{3,2}$		$a_{3,3}$	
Study Sites	Soil ID	%	Soil ID	%	Soil ID	%	Soil ID	%	Soil ID	%	Soil ID	%	Soil ID	%	Soil ID	%	Soil ID	%
LW 13	3	10.0	2	10.0	3	6.7	3	16.7	2	3.3	2	6.7	2	3.3	2	3.3	2	3.3
	6	**23.3**	3	30.0	**6**	**23.3**	**6**	**36.7**	3	6.7	3	10.0	3	23.3	3	6.7	3	3.3
	8	**63.3**	**6**	**30.0**	**8**	**66.7**	**8**	**46.6**	**6**	**33.3**	**6**	**40.0**	**6**	**16.7**	**6**	**30.0**	**6**	**26.7**
	21	3.4	**8**	**30.0**	10	3.3			**8**	**50.0**	**8**	**43.3**	**8**	**56.7**	**8**	**56.7**	**8**	**56.7**
									21	6.7					21	3.3	10	6.7
																	21	3.3
	Sum	100		100		100		100		100		100		100		100		100
LW 21	**9**	**43.3**	**9**	**30.0**	**12**	**26.7**	14	50.0	5	13.3	2	33.3	**9**	**73.3**	**9**	**53.3**	1	13.3
	5	6.7	1	10.0	2	16.7	**9**	**43.3**	**9**	**30.0**	**12**	**20.0**	14	23.3	1	23.3	2	10.0
	14	43.3	2	23.3	**9**	**26.7**	3	3.3	1	20.0	1	23.3	1	3.4	5	6.7	5	10.0
	13	3.3	**12**	**13.3**	1	16.7	1	3.4	**12**	**23.3**	**9**	**13.4**			**12**	**13.3**	**9**	**43.3**
	1	3.4	5	20.0	5	6.7			2	13.4	**7**	**3.3**			2	3.4	**12**	**23.4**
			7	**3.4**	3	3.3					5	3.3						
					7	**3.4**					14	3.4						
	Sum	100		100		100		100		100		100		100		100		100

[a]See Table 1 for soil identification (soil ID) values from the physical soil texture database. Bold: the exact solution searched.

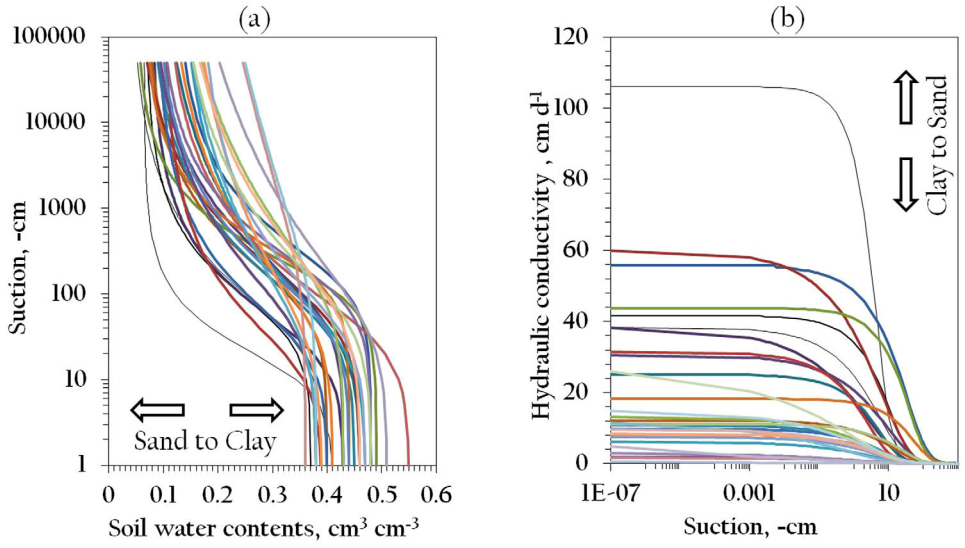

Figure 11. (a) Soil water contents ($\theta(h)$) and (b) hydraulic conductivities ($K(h)$) of physical soil texture database.

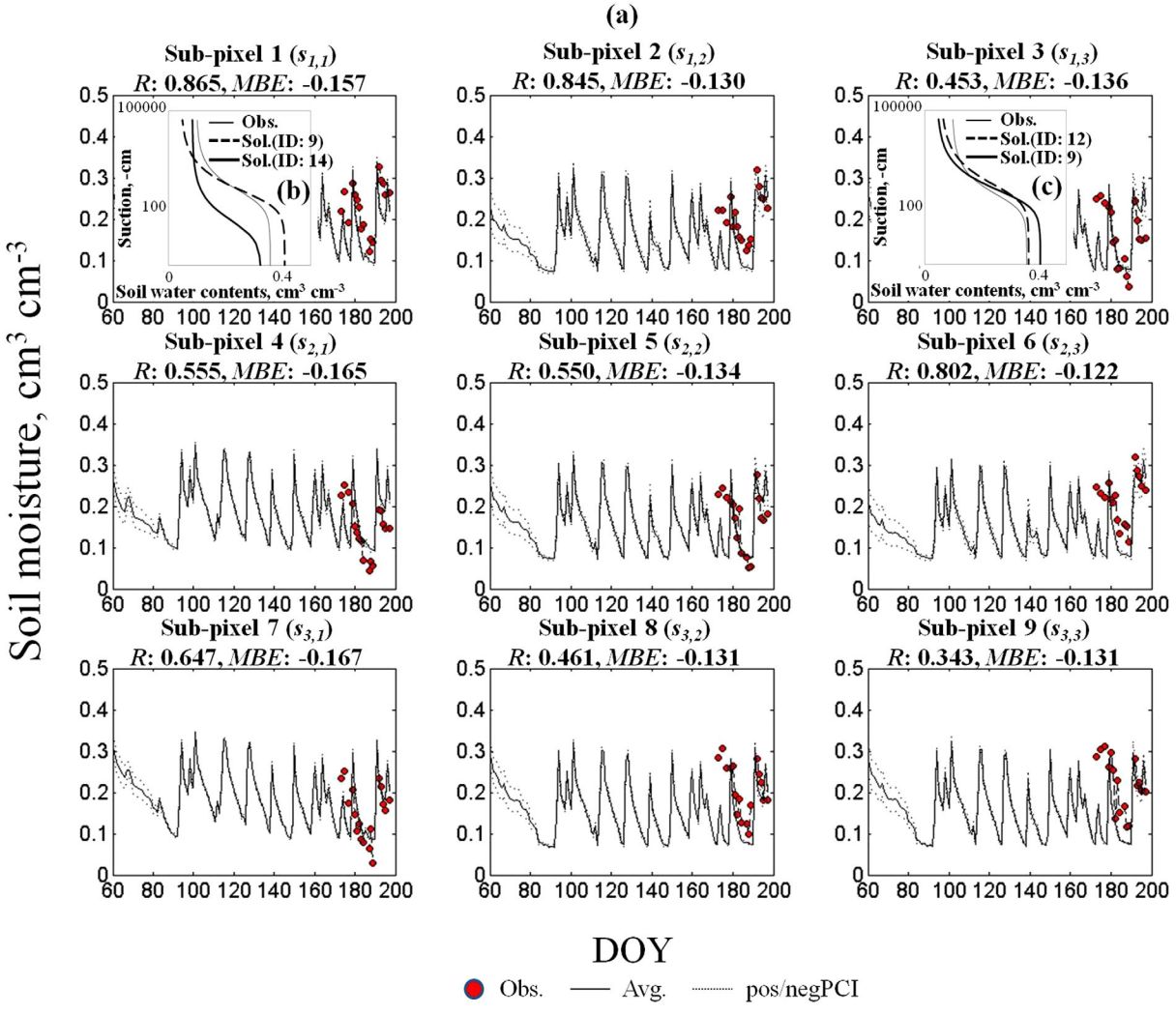

Figure 12. (a) Soil moisture dynamics (0–5 cm) of subpixels downscaled by the deterministic downscaling algorithm using the genetic algorithm (EMOGA) at the LW 21 site in Oklahoma, (b) $\theta(h)$ functions of the observation and solutions (soil ID: 9, 14), and (c) $\theta(h)$ functions of the observation and solutions (soil ID: 9, 12).

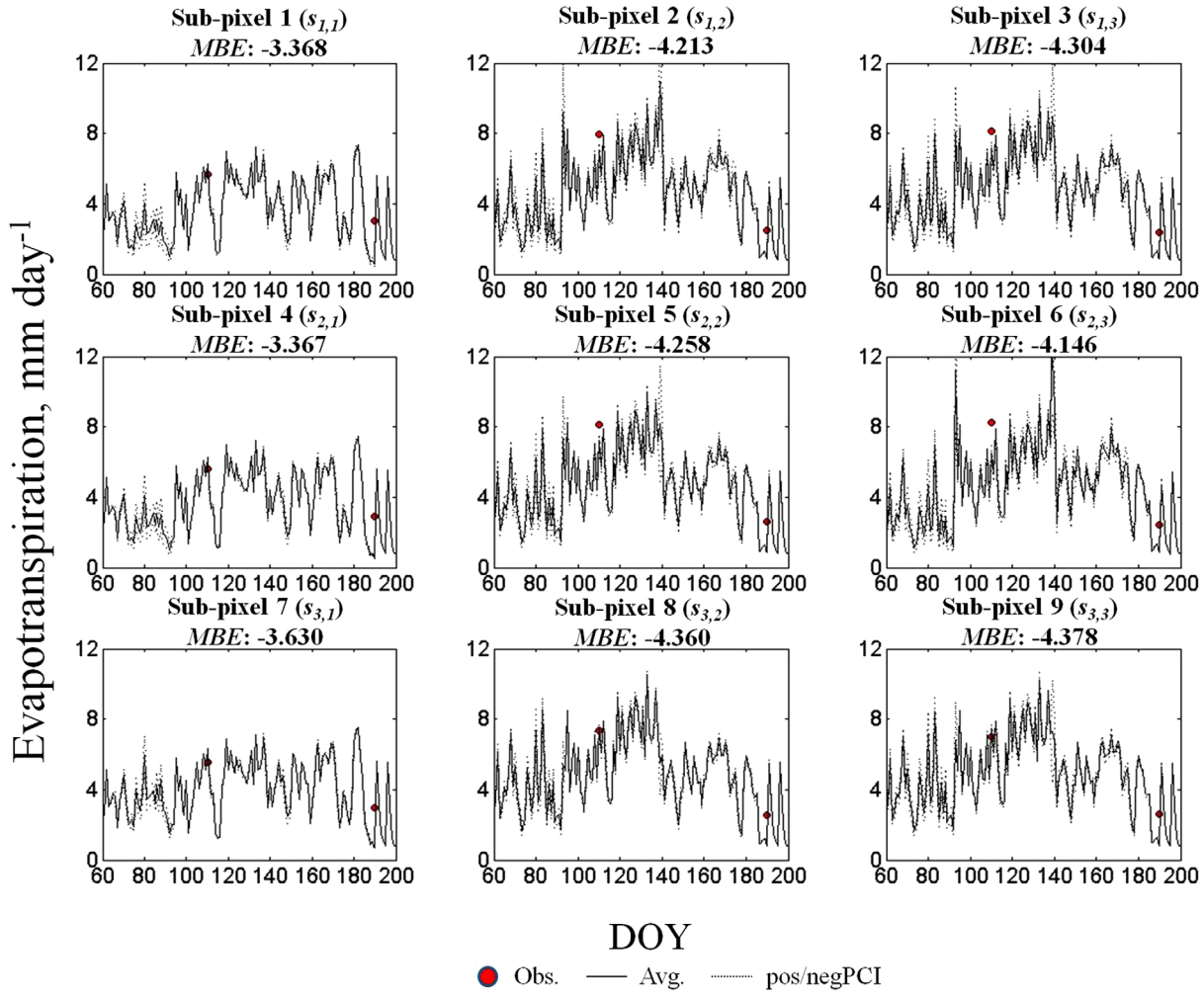

Figure 13. Evapotranspiration of subpixels by the deterministic downscaling algorithm using the genetic algorithm (EMOGA) at the LW 21 site in Oklahoma.

soil moisture from the remotely sensed (RS) soil moisture (SM) and evapotranspiration (ET) products based on inverse modeling under different hydro-climatic regions. We extracted the pixel-based soil ID values (representing soil textures) of subpixels within the RS pixel and simulated the long-term SM and ET dynamics through the hydrological model using the searched (soil ID) results of subpixels. Synthetic experiments were conducted under various (simple, relatively simple, relatively complex, and complex) land surface conditions with different vegetation covers (wheat, soybean, grass, and maize) and shallow ground water tables (−100, −150, and −200 cm), respectively. Then, we validated the applicability of this approach with the in situ soil moisture measurements and $\theta(h)$ curves derived by the soil hydraulic parameters obtained from the soil core samples collected at the field (LW 13 and 21) sites in Oklahoma.

[33] The synthetic cases showed the robustness of the algorithm for extracting the soil ID values of subpixels. Under the simple, relatively simple, relatively complex, and complex land surface conditions, this approach fairly identified the solutions of subpixels, although uncertainties were included in the derived solutions. Land covers had more impacts on the model performance than the presence of shallow ground water tables. In the field experiments, the downscaled soil moisture estimates of subpixels (from ESTAR footprint) showed the moderate correlation (R: 0.724–0.914, MBE: −0.203 to −0.169 for LW 13; R: 0.343–0.865, MBE: −0.165 to −0.122 for LW 21) with the in situ measurements. Mostly, DDA searched loam, silt, and silt loam soils (soil ID: 6, 8, 7, 9, 12) as dominant soils at the individual subpixels compared to the observations (predominantly loam and silt loam) at the LW 13 and 21 sites. Although there exist uncertainties due to the non-uniqueness of solutions (e.g., similarities of soil hydraulic responses among the soil textures included in the physical soil texture database, colinearity of covariates, inherent weakness of hydrological model structures, and errors in measurements and initial/bottom boundary conditions) and few pixel-based ET measurements available, the results

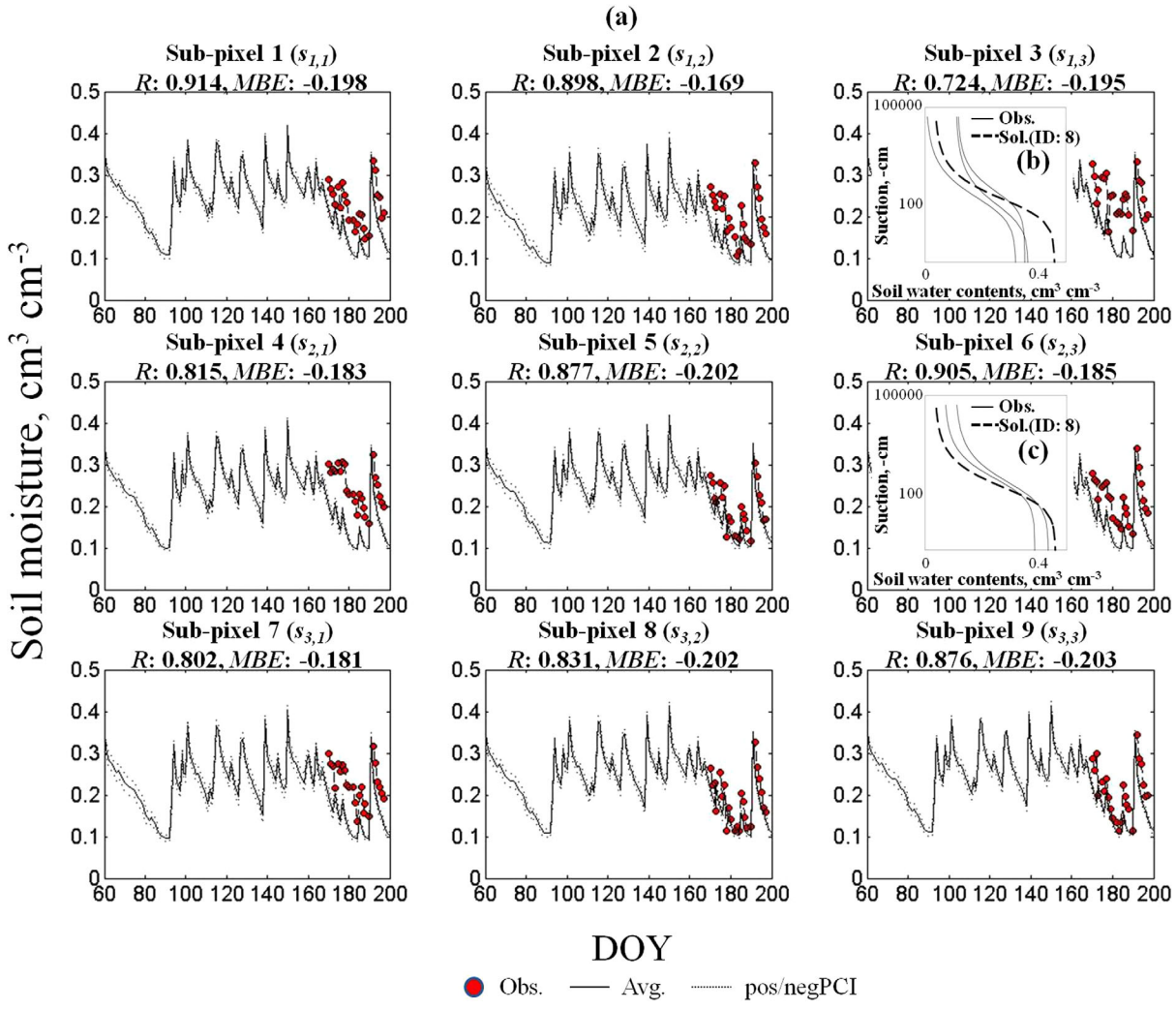

Figure 14. (a) Soil moisture dynamics (0–5 cm) of subpixels downscaled by the deterministic downscaling algorithm using the genetic algorithm (EMOGA) at the LW 13 site in Oklahoma, (b) $\theta(h)$ functions of the observation and solutions (soil ID: 8), and (c) $\theta(h)$ functions of the observation and solutions (soil ID: 8).

show good performance of the approach. In other words, the soil moisture estimates downscaled by the deterministic downscaling algorithm matched well with the generated observations under synthetic conditions and field measurements during the SGP97 hydrology experiment. The good match of observed (field-observed soil hydraulic properties) and simulated (derived-soil ID values) $\theta(h)$ functions supports the robustness of our approach further in downscaling the RS products at the airborne footprint scales. On the basis of these findings, we suggest that the deterministic downscaling algorithm with the genetic algorithm (EMOGA) can be useful for downscaling the remotely sensed soil moisture products at the spatiotemporal scales using the pixel-based evapotranspiration. Also, we could condition our approach selectively for providing disaggregated results in the spatial or temporal domain only. It will greatly assist in providing model outputs that can meet various users' need. However, the disaggregation algorithm might be limited due to the environmental factors (i.e., qualities of RS soil moisture and evapotranspiration, weather forcings/conditions, soils, vegetations, etc.) indicating that the use of qualified input data under appropriate weather conditions is required. Currently, downscaling satellite-scale soil moisture footprints (i.e., SMOS or SMAP, 40 km × 40 km, AMSR-E, 25 km × 25 km, etc.) was not tested in this study due to the lack of detailed finer scale soil moisture data, and the limited computation ability in the model performance on the PC environment, etc. within the large footprints currently. However, our proposed algorithm can be extended to disaggregate satellite-scale soil moisture products with subpixel levels ranging several hundred meters to kilometers. Thus, these products

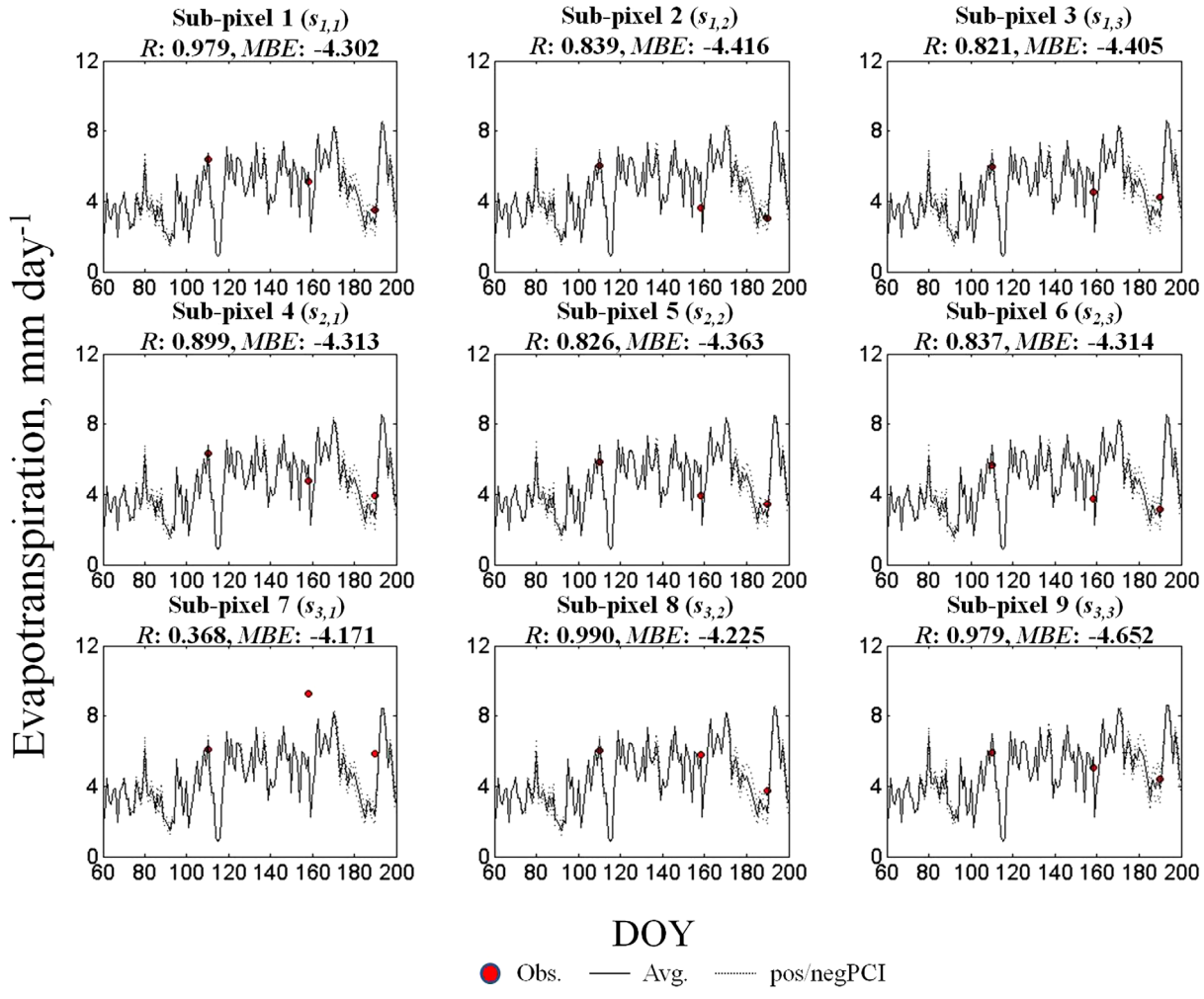

Figure 15. Evapotranspiration of subpixels by the deterministic downscaling algorithm using the genetic algorithm (EMOGA) at the LW 13 site in Oklahoma.

could be further evaluated for improvement in modeling skills in the context of land-atmosphere interaction, hydrology, and general circulation.

[34] **Acknowledgments.** The research was partially funded by NASA-THP grants (NNX08AF55G, NNX09AK73G) and NSF (CMG/DMS) grants (0621113, 0934837).

References

Allen, R. G., M. Tasumi, and R. Trezza (2007), Satellite-based energy balance for mapping evapotranspiration with internalized calibration (METRIC): Model, *ASCE J. Irrig. Drain. Eng*., *133*(4), 380–394.

Bastiaanssen, W. G. M., M. Menenti, R. A. Feddes, and A. A. M. Holtslag, (1998), A remote sensing surface energy balance algorithm for land (SEBAL). I. Formulation, *J. Hydrol*., 212–213, 198–212.

Bastiaanssen, W. G. M., E. J. M.Noordman, H. Pelgrum, G. Davids, B. P. Thoreson, and R. G. Allen (2005), SEBAL model with remotely sensed data to improve water-resources management under actual field criterion, *J. Irrig. Drain. Eng. ASCE*., *131*(1), 85–93.

Boulet, G., I. Braud, and M. Vauclin (1997), Study of the mechanisms of evaporation under arid conditions using a detailed model of the soil-atmosphere continuum: Applications to the EFEDA I experiment, *J. Hydrol.*, *193*, 114–141.

Chauhan, N., S. Miller, and P. Ardanuy (2003), Spaceborne soil moisture estimation at high resolution: A microwave-optical/IR synergistic approach, *Int. J. Remote Sens.*, *24*(22), 4599–4622.

Crow, W. T., E. F. Wood, and R. Dubayah (2000), Potential for downscaling soil moisture maps derived from space borne imaging radar data, *J. Geophys. Res.*, *105*, 2203–2212.

Das, N. N., B. P. Mohanty, and E. G. Njoku (2008), Characterization of backscatter by surface features in L-band active microwave remote sensing of soil moisture, *IEEE Trans. Geosci. Remote Sens.*, *2*, 817–820, doi:10.1109/IGARSS.2008.4779119.

Das, N. N., D. Entekhabi, and E. Njoku (2011), An algorithm for merging SMAP radiometer and radar data for high resolution soil moisture retrieval, *IEEE Trans. Geosci. Remote Sens.*, *49*(5), 1504–1512, doi:10.1109/TGRS.2010.2089526.

Droogers, P., W. G. M. Bastiaanssen, M. Beyazgül, Y. Kayam, G. W. Kite, and H. Murray-Rust (2000), Distributed agro-hydrological modeling of an irrigation system in western Turkey, *Agric. Water Manage.*, *43*(2), 183–202, doi:10.1016/S0378–3774 (99)00055–4.

Efron, B. (1982), *The Jackknife, the Bootstrap and Other Resampling Plans*, Soc. for Ind. and Appl. Math., Philadelphia, Pa.

Engman, T. (1991), Application of microwave remote sensing of soil moisture for water resources and agriculture, *Remote Sens. Environ.*, *35*, 213–226.

Entekhabi, D., G. R. Asrar, A. K. Betts, K. J. Beven, R. L. Bras, and C. J. Duffy (1999), An agenda for land surface hydrology research and a call for the second international hydrological decade, *Bull. Am. Meteorol. Soc.*, *80*(10), 2043–2058.

Entekhabi, D., et al. (2010), The soil moisture active passive (SMAP) mission, *Proc. IEEE*, *98*(5), 704–716.

Ferreira, M. E., L. G. Ferreira, E. E. Sano, and Y. E. Shimabukuro (2007), Spectral linear mixture modeling approaches for land cover mapping of tropical savanna areas in Brazil, *Int. J. Remote Sens.*, *28*(2), 413–429, doi:10.1080/01431160500181507.

Feddes, R. A., P. J. Kowalik, and H. Zarandy (1978), *Simulation of Field Water Use and Crop Yield*, John Wiley, New York.

Goldberg, D. E. (1989), *Genetic Algorithms in Search and Optimization and Machine Learning*, Addison-Wesley, New York.

Holben, B. N., and Y. E. Shimabukuro (1993), Linear mixing applied to coarse spatial resolution data from multispectral satellite sensors, *Int. J. Remote Sens.*, *14*, 2231–2240.

Holland, J. H. (1975), *Adaptation in Natural and Artificial System*, University of Michigan press, Ann Arbor, Mich.

Huxman, T., B. P. Wilcox, D. D. Breshears, R. L. Scott, K. A. Snyder, E. E. Small, K. Hultine, W. T. Pockman, and R. B. Jackson (2005), Ecohydrological implications of woody plant encroachment, *Ecology*, *86*(2), 308–319.

Ines, A. V. M., and P. Droogers (2002), Inverse modeling in estimating soil hydraulic functions: A genetic algorithm approach, *Hydrol. Earth Syst. Sci.*, *6*(1), 49–65.

Ines, A. V. M., and K. Honda (2005), On quantifying agricultural and water management practices from low spatial resolution RS data using genetic algorithms: A numerical study for mixed-pixel environment, *Adv. Water Resour.*, *28*, 856–870.

Ines, A. V. M., and B. P. Mohanty (2008a), Near-surface soil moisture assimilation to quantify effective soil hydraulic properties using genetic algorithm: I. Conceptual modeling, *Water Resour. Res.*, *44*, W06422, doi:10.1029/2007WR005990.

Ines, A. V. M., and B. P. Mohanty (2008b), Parameter conditioning with a noisy Monte Carlo genetic algorithm for estimating effective soil hydraulic properties from space, *Water Resour. Res.*, *44*, W08441, doi:10.1029/2007WR006125.

Ines, A. V. M., and B. P. Mohanty (2009), Near-surface soil moisture assimilation for quantifying effective soil hydraulic properties using genetic algorithms: II. Using airborne remote sensing dyring SGP97 and SMEX02, *Water Resour. Res.*, *45*, W01408, doi:10.1029/2008WR007022.

Ines, A. V. M., B. P. Mohanty, and Y. Shin (2013), An un-mixing algorithm for remotely sensed soil moisture, *Water Resour. Res.*, *49*, 408–425, doi:10.1029/2012WR012379.

Jackson, T. J., D. M. Le Vine, A. Y. Hsu, A. Oldak, and P. J. Starks (1999), Soil moisture mapping at regional scales using microwave radiometry: The southern Great Plains hydrology experiment, *IEEE Trans. Geosci. Remote Sens.*, *37*(5), 2136–2151.

Kerr, Y. H., P. Waldteufel, J. P. Wigneron, J. M. Martinuzzi, J. Font, and M. Berger (2001), Soil moisture retrieval from space: The soil moisture and ocean salinity (SMOS) mission, *IEEE Trans. Geosci. Remote Sens.*, *39*(8), 1729–1735.

Kim, G., and A. P. Barros (2002), Downscaling of remotely sensed soil moisture with a modified fractal interpolation method using contraction mapping and ancillary data, *Remote Sens. Environ.*, *83*, 400–413.

Kroes, J. G., J. C. van Dam, J. Huygen, and R. W. Vervoort (1999), User's guide of SWAP version 2.0: Simulation of water, solute transport, and plant growth in the soil-atmosphere-plant environment, Rep. 81, DLO Winand Staring Cent., Wageningen, Netherlands.

Leij, F. J., W. J. Alves, M. T. van Genuchten, and J. R. Williams (1999), The UNSODA unsaturated soil hydraulic database, in *Proceeding of International Workshop on Characterization and Measurement of the Hydraulic Properties of Unsaturated Porous Media*, edited by M. T. van Genuchten and F. J. Leij, pp. 1269–1281, Univ. of Calif., Riverside.

Mascaro, G., E. R. Vivoni, and R. Deidda (2010), Downscaling soil moisture in the southern Great Plains through a calibrated multifractal model for land surface modeling applications, *Water Resour. Res.*, *46*, W08546, doi:10.1029/2009WR008855.

Merlin, O., G. Chehbouni, Y. Kerr, E. G. Njoku, and D. Entekhabi (2005), A combined modeling and multi-spectral/multi-resolution remote sensing approach for disaggregation of surface soil moisture: Application to SMOS configuration, *IEEE Trans. Geosci. Remote Sens.*, *43*(9), 2036–2050, doi:10.1109/tgrs.2005.853192.

Merlin, O., J. Walker, A. Chehbouni, and Y. Kerr (2008), Towards deterministic downscaling of SMOS soil moisture using MODIS derived soil evaporative efficiency, *Remote Sens. Environ.*, *112*, 3935–3946, doi:10.1016/j.rse.2008.06.012.

Merlin, O., C. Rudiger, A. Al Bitar, J. P. Walker, and Y. H. Kerr (2012), Disaggregation of SMOS soil moisture in southeastern Australia, *IEEE Trans. Geosci. Remote Sens.*, *50*(5), 1556–1571.

Mohanty B. P., and T. H. Skaggs (2001), Spatio-temporal evolution and time-stable characteristics of soil moisture within remote sensing footprints with varying soil, slope, and vegetation, *Adv. Water Resour.*, *24*, 1051–1067.

Mohanty, B. P., P. J. Shouse, D. A. Miller, and M. T. van Genuchten (2002), Soil property database: Southern Great plains 1997 hydrology experiment, *Water Resour. Res.*, *38*(5), 1047, doi:10.1029/2000WR000076.

Moran, M. S., S. J. Maas, and P. J. Pinter Jr. (1995), Combining remote sensing and modeling for estimating surface evaporation and biomass production, *Remote Sens. Rev.*, *12*, 335–353.

Moulin, S., A. Bondeau, and R. Delécolle (1998), Combining agricultural crop models and satellite observations: From field to regional scales, *Int. J. Remote Sens.*, *19*(6), 1021–1036.

Mualem, Y. (1976), A new model for predicting the hydraulic conductivity of unsaturated porous media, *Water Resour. Res.*, *12*, 513–522.

Njoku, E., and D. Entekkabi (1996), Passive microwave remote sensing of soil moisture, *J. Hydrol.*, *184*, 101–129.

Njoku, E. G., T. L. Jackson, V. Lakshmi, T. Chan, and S. V. Nghiem (2003), Soil moisture retrieval from AMSR-E, *IEEE Trans. Geosci. Remote Sens.*, *41*, 215–229.

Ottlé, C., and D. Vidal-Madjar (1994), Assimilation of soil moisture inferred from infrared remote sensing in a hydrological model over the HAPEX-MOBILHY region, *J. Hydrol.*, *158*, 241–264.

Piles, M., et al. (2010), Soil moisture downscaling activities at the REMEDHUS Cal/Val site and its application to SMOS, *IEEE 11th Special Meeting on Microwave Radiometry and Remote Sensing of the Environment,* pp. 17–21, MicroRad, Washington, D. C., doi:10.1109/MICRORAD.2010.5559599.

Piles, M., A. Camps, M. Vall-llossera, I. Corbella, R. Panciera, C. Rüdiger, Y. H. Kerr, and J. Walker (2011), Downscaling SMOS-derived soil moisture using MODIS visible/infrared data, *IEEE Trans. Geosci. Remote Sens.*, *49*(9), 3156–3166.

Pollacco, J. A., and B. P. Mohanty (2012), Uncertainties of water fluxes in SVAT models: Inverting surface soil moisture and evapotranspiration retrieved from remote sensing, Special Section on Soil–Plant–Atmosphere Continuum, *Vadose Zone J.*, 11, doi:10.2136/vzj2011.0167.

Roerink, G. J., Z. Su, and M. Menenti (2000), S-SEBI: A simple remote sensing algorithm to estimate the surface energy balance, *Phys. Chem. Earth*, *25*(2), 147–157.

Sarwar, A., W. G. M. Bastiaanssen, M. T. Boers, and J. C. van Dam (2000), Evaluating drainage design parameters for the fourth drainage project, Pakistan by using SWAP model: I. Calibration, *Irrig. Drain. Syst.*, *14*(4), 257–280, doi:10.1023/A:1006468905194.

Schaap, M. G., F. J. Leij, and M. T. van Genuchten (1999), A bootstrap-neural network approach to predict soil hydraulic parameters, in *Proceeding of International Workshop on Characterization and Measurement of the Hydraulic Properties of Unsaturated Porous Media*, edited by M. T. van Genuchten and F. J. Leij, pp. 1237–1250, Univ. of California, Riverside.

Shin, Y., B. P. Mohanty, and A. V. M. Ines (2012), Soil hydraulic properties in one-dimensional layered soil profile using layer-specific soil moisture assimilation scheme, *Water Resour. Res.*, *48*, W06529, doi:10.1029/2010WR009581.

Shin, Y., B. P. Mohanty, and A. V. M. Ines (2013), Estimating effective soil hydraulic properties using spatially distributed soil moisture and evapotranspiration products at multiple scales, *Vadose Zone J.*, *12*, doi:10.2136/vzj2012.0074.

Singh, R., R. K. Jhorar, J. C. van Dam, and R. A. Feddes (2006), Distributed ecohydrological modeling to evaluate irrigation system performance in Sirsa district, India: II. Impact of viable water management scenarios, *J. Hydrol.*, *329*, 714–723, doi:10.1016/j.jhydrol.2006.03.016.

Su, Z. (2002), The surface energy balance system (SEBS) for estimation of turbulent heat fluxes, *Hydro. Earth Sys. Sci*., *6*, 85–99.

Supit, I., A. A. Hooyer, and C. A. van Diepen (1994), System Description of the WOFOST 6.0 Crop Simulation Model Implemented in GCMS, Volume 1: Theory and Algorithms, Joint Res. Cent., Comm. of the Eur. Commun., Luxembourg.

Ulaby, F., P. Dubois, and J. von Zyl (1996), Radar mapping of surface soil moisture, *J. Hydrol.*, *184*, 57–84.

van Dam, J. C. (2000), Field-scale water flow and solute transport: SWAP model concepts, parameter estimation, and case studies, PhD dissertation, Dep. of Soil Phys., Agric. Hydrol. and Groundwater, Wageningen Univ., Wageningen, Netherlands.

van Dam, J. C., J. Huygen, J. G. Wesseling, R. A. Feddes, P. Kabat, P. E. V. van Waslum, P. Groenendjik, and C. A. van Diepen (1997), Theory of SWAP version 2.0: Simulation of water flow and plant growth in the

soil-water-atmosphere-plant environment, *Tech. Doc. 45*, DLO Winand Staring Cent., Wageningen, Netherlands.

van Genuchten, M. T. (1980), A closed-form equation foe predicting the hydraulic conductivity of unsaturated soils, *Soil Sci. Soc. Am. J.*, *44*(5), 892–898.

van Keulen, H., and D. Hillel (1974), A simulation study of the drying-front phenomenon, *Soil Sci.*, *118*, 270–273.

Walker, J. P., G. R. Willgoose, and J. T. Kalma (2001), One-dimensional soil moisture profile retrieval by assimilation of near-surface observations: A comparison of retrieval methods, *Adv. Water Resour.*, *24*, 631–650, doi:10.1016/S0309-1708(00)00043-9.

Wesseling, J. G., and J. G. Kroes (1998), A global sensitivity analysis of the model SWAP, *Rep. 160*, DLO Winand Staring Cent., Wageningen, Netherlands.

Wösten, J. H. M., G. H. Veerman, and J. Stolte (1994), Water retention and hydraulic conductivity functions of top- and sub-soils in the Netherlands: The staring series, *Tech. Doc. 18*, DLO Winand Staring Cent., Wageningen, Netherlands.

Xevi, E., J. Gilley, and J. Jeyen (1996), Comparative study of two crop yield simulation models, *Agric. Water Manage.*, *30*, 155–173.

Yamanaka, T., and T. Yonetani (1999), Dynamics of the evaporation zone in dry sandy soils, *J. Hydrol.*, *217*, 135–148.